Journal of Materials Chemistry C

ROYAL SOCIETY OF CHEMISTRY

PAPER

View Article Online
View Journal | View Issue

Cite this: J. Mater. Chem. C, 2025, 13, 18492

Rapid microwave-assisted synthesis of morphology-controlled luminescent lanthanide-doped Gd_2O_2S nanostructures

Christian Homann, †[a] Régis Peeters,[a] Hana Mirmajidi,[a] Jessica Berg,[a] Michael Fay,[b] Lucas Carvalho Veloso Rodrigues,[c] Eros Radicchi,[d] Akhil Jain,[e] Adolfo Speghini[f] and Eva Hemmer*[a]

Gadolinium oxysulfide (Gd_2O_2S) is an attractive material of demonstrated suitability for a variety of imaging applications, leveraging its magnetic, scintillating, and luminescent properties, particularly when doped with optically active lanthanide ions (Ln^{3+}). For many of these applications, control over size and morphology at the nanoscale is crucial. This study demonstrates the rapid microwave-assisted synthesis of colloidal Ln_2O_2S (Ln = Gd and dopants Yb, Er, Tb) nanostructures in as little as 20 min. Structural characterization using X-ray diffraction analysis (XRD), Raman spectroscopy, as well as transmission electron microscopy (TEM), including elemental mapping *via* energy dispersive X-ray spectroscopy (EDS), unveiled the key role of elemental sulphur (S_8) in the reaction mixtures for materials growth. By systematically varying the Ln-to-S ratio from 1 : 0.5 to 1 : 15, controlled morphologies ranging from triangular nanoplatelets to berry- and flower-like shapes were achieved. Doping with Er^{3+}/Yb^{3+} endowed the nano-triangles with upconverting and near-infrared emitting properties. Tb^{3+}-doped Gd_2O_2S exhibited the characteristic green Tb^{3+} emission under UV excitation, while also showing X-ray excited optical luminescence (XEOL), rendering the material interesting as a potential nano-scintillator.

Received 24th April 2025,
Accepted 4th August 2025

DOI: 10.1039/d5tc01646k

rsc.li/materials-c

Introduction

Due to their scintillating properties, lanthanide oxysulfides (Ln_2O_2S) are well-known for their application in X-ray screens, allowing for the conversion of high-energy radiation into visible light for imaging purposes.[1–4] However, interest in their optical properties is on a constant rise given their high chemical stability along with low photobleaching as well as low phonon energy. Of particular interest with respect to the development of phosphors is the suitability of Gd_2O_2S to act as a host matrix for dopant ions such as Yb^{3+}/Er^{3+}, Yb^{3+}/Tm^{3+}, Eu^{3+} or Tb^{3+}, which endow the material with upconverting and downshifting properties, or Ti and Mg^{2+} to induce persistent luminescence.[4–7] Herein, Gd_2O_2S also benefits from the paramagnetic behaviour of the Gd^{3+} ion, making it a potential candidate for magnetic resonance imaging (MRI) applications.[8–10]

Seeking efficient upconverters, microcrystalline Gd_2O_2S doped with 10 mol% Er^{3+} was demonstrated to efficiently upconvert longer-wavelength near-infrared (NIR) to shorter-wavelength NIR light, when excited with 1510 nm, targeting the $^4I_{13/2}$ level of Er^{3+}.[5,11] Remarkably, the internal upconversion quantum yield of the microcrystalline Gd_2O_2S reached 12%, which outperformed that of Er^{3+}-doped β-$NaYF_4$. With the increasing interest in optical thermal sensing based on the temperature-dependent spectral features of the Ln^{3+} ions, recent work explored the potential of Gd_2O_2S as a luminescent thermometer. For example, Ma *et al.* reported a new dual functionality luminescence thermometer based on microcrystalline Gd_2O_2S co-doped with Eu^{3+} and Nd^{3+}, which combined Boltzmann and energy transfer thermometry to extend the applicable temperature range.[12] Work by Pessoa *et al.* showcases the suitability of Er^{3+} and Yb^{3+} co-doped Gd_2O_2S nanoparticles (NPs) for nanothermometry under bichromatic

[a] Department of Chemistry and Biomolecular Sciences, University of Ottawa, Ottawa (ON) K1N 6N5, Canada. E-mail: ehemmer@uottawa.ca
[b] Nanoscale and Microscale Research Centre & Faculty of Engineering, University of Nottingham, Nottingham, NG7 2RD, UK
[c] Department of Fundamental Chemistry, Institute of Chemistry, University of São Paulo, Av. Prof. Lineu Prestes 748, São Paulo-SP, 05508-000, Brazil
[d] Department of Engineering DIMI, University of Verona, Strada Le Grazie 15, 37134 Verona, Italy
[e] Bioelectronics Laboratory, Division of Pharmacy & Optometry, Faculty of Biology, Medicine and Health, University of Manchester, Oxford Road, Manchester, M13 9PTL, UK
[f] Nanomaterials Research Group – Department of Biotechnology, University of Verona, Strada Le Grazie 15, 37134 Verona, Italy
† Current affiliation: Division Biophotonics, Federal Institute for Materials Research and Testing (BAM), Richard-Willstaetter-Str. 11, Berlin, D-12489, Germany.

excitation, *i.e.*, 859 nm and 1510 nm.[13] Zou *et al.* proposed a core/shell architecture based on a Ln^{3+}-doped Gd_2O_2S core and a $NaYF_4$ shell, whereas changes in the lattice strain were proposed as the origin for the observed variation of the luminescence intensity ratio as a function of temperature.[14] Other innovative applications of microscale Gd_2O_2S particles include tracer-based sorting, a technique that uses trace amounts of inorganic phosphors for, *e.g.*, sorting plastics based on criteria beyond plastic type. In this context, Cosgun Ergene *et al.* investigated the synergistic effect of co-doping Gd_2O_2S with Ce^{3+} to enhance Er^{3+} luminescence at *ca.* 1550 nm (with a maximum quantum yield of 5.7%) and developed an extended range of unique tracer combinations.[15] These studies are excellent examples that showcase the outstanding properties of Ln_2O_2S. Leveraging these properties, over the past years, the suitability of Ln_2O_2S for use in optoelectronic devices, as bio labels or regenerator material, among others, has been demonstrated.[16–21]

However, the synthesis of Ln_2O_2S still poses significant challenges, particularly when aiming for nanoscale materials. The conventional preparation of Ln_2O_2S typically involves solid-state reactions, which require high temperatures and annealing steps in a sulphur-containing atmosphere. For instance, the sulphuration, *i.e.*, annealing at high temperature for several hours in the presence of sulphur under an argon gas flow or in the presence of an Ar–H_2S atmosphere or urea as sulphur source, of lanthanide oxides, hydrocarbonates, or nitrates, was reported to yield Ln_2O_2S nanospheres of *ca.* 100 nm or nanospindles.[8,10,13,21] Alternatively, Ln_2O_2S sub-micron particles were obtained *via* pyrolysis of a molecular precursor cocktail, containing the required elements[22] or *via* solvothermal synthesis.[23] With the desire for colloidal NPs of homogenous size distribution, strategies based on the thermal decomposition of suitable precursors in an organic medium were developed as promising alternative to conventional solid-state reactions.[7,24–26] Herein, elemental sulphur (S_8) can be employed as the sulphur source, which is of interest due to its simplicity.[4,27] An alternative strategy is based on the *in situ* release of sulphur during the thermal decomposition of S-containing molecules, such as CS_2,[25] Ln[(phen)(ddtc)$_3$] (phen = 1,10-phenanthroline; ddtc = diethyldithiocarbamate)[26,28] or *N*,*N*′-diphenylthiourea (DPTU).[14,20] Importantly, studies by Larquet *et al.* and Zou *et al.* unveiled the importance of the addition of mineralizers, *i.e.*, Na^+ or Li^+ ions.[20,27]

Most of these examples showcase the synthesis of spherical NPs. Yet, interestingly, various other morphologies beyond spheres have been reported for Ln_2O_2S, including nanorods, -belts, -tubes, and -wires, as well as sheets, and hexagonal shaped crystals.[29–31] In that regard, recent work by Yorov *et al.* is noteworthy.[4] The authors reported the morphological evolution of colloidal Gd_2O_2S:Tb^{3+} nanomaterials. Using a modified thermal decomposition approach, employing S_8 and Ln acetylacetonate as precursors, morphological control from flower-like shape to circles and hexagonal-shaped nanoplatelets was achieved over the course of 30 h.

Microwave-induced heating is an interesting alternative to conventional, convectional heating as it offers a shortened and more homogeneous heating process, which has the potential to favour the growth of monodisperse (nano)materials.[32,33] To the best of our knowledge, no solution-based microwave-assisted synthesis of Ln_2O_2S NPs has been reported to date. However, the synthesis of Ln_2O_2S *via* microwave-assisted solid-state synthesis has been demonstrated.[6,34–36] This approach comes with fast reaction times, *e.g.*, as short as 10 min;[35] though, the obtained materials are of rather heterogenous size distribution at the (sub)micron-scale.

Thus, while achievements have been made over the past years, synthetic strategies that yield monodisperse, colloidal Ln_2O_2S NPs in a fast and straightforward manner, not requiring annealing in a S-atmosphere or complex precursors remain scarce. To address this gap, inspired by previous work reporting colloidal Ln_2O_2S *via* thermal decomposition and our previous studies on the straightforward microwave-assisted synthesis of $NaLnF_4$ NPs,[37,38] we here demonstrate for the first time the solution-based microwave-assisted synthesis of colloidal Ln_2O_2S nanomaterials. Herein, we exploit the advantages of microwave-induced heating in a closed vessel over conventional, convectional heating, which comes with significantly shortened reactions times, *i.e.*, minutes *versus* hours. Moreover, we focused on precursor choices that allowed for use without additional purification or synthetic steps. Therefore, lanthanide acetates (Ln(OAc)$_3$), which can easily be dissolved in the solvent mixture of oleic acid (OA), 1-octadecene (ODE), and oleylamine (OAm), were used as lanthanide source. Elemental sulphur powder (S_8) was used as a convenient, readily available source for sulphur. An in-depth structural and morphological study was conducted to unveil the formation mechanism of Ln_2O_2S under microwave irradiation. Herein, in addition to reaction time, the lanthanide-to-sulphur (Ln-to-S) and sodium-to-lanthanide (Na-to-Ln) ion ratios were identified as crucial for morphology control. More specifically, by tuning the metal ion ratio within the reaction mixture, colloidal triangular-shaped Ln_2O_2S nanoplatelets (nano-triangles) as well as raspberry- and flower-like nanostructures were obtained in as little as 10 to 20 min of microwave irradiation. Assessing the potential of the obtained materials as optical probes, doping with Er^{3+}/Yb^{3+} as well as Tb^{3+} endowed the Gd_2O_2S nanostructures with photoluminescence in the visible and NIR spectral region as well as X-ray excited optical luminescence (XEOL).

Experimental section

Materials

Gadolinium oxide (Gd_2O_3, 99.999%), ytterbium oxide (Yb_3O_3, 99.998%), and erbium oxide (Er_2O_3, 99.99%) were purchased from Alfa Aesar. Terbium oxide (Tb_2O_3, 99.99%), oleic acid ($CH_3(CH_2)_7CH{=}CH(CH_2)_7COOH$, OA, 90%), oleylamine ($CH_3(CH_2)_7CH{=}CH(CH_2)_7CH_2NH_2$, OAm, 70%), 1-octadecene ($CH_3(CH_2)_{15}CH{=}CH_2$, ODE, 90%), sodium oleate ($CH_3(CH_2)_7CH{=}CH(CH_2)_7COONa$, NaOA, $\geq$82%), and sulphur (S, reagent grade) were purchased from Sigma Aldrich. Ethanol (99%) was purchased from Commercial Alcohols. Acetone and hexane (analytical grade) were purchased from

Fischer Chemicals. Toluene (99.8%) was purchased from Fisher Scientific. All chemicals were used as received.

Microwave-assisted synthesis of $Gd_2O_2S:Er^{3+}/Yb^{3+}$ as well as $Gd_2O_2S:Tb^{3+}$ and $Gd_2O_2S:Tb^{3+}/Yb^{3+}$

For the microwave-assisted synthesis of Gd_2O_2S co-doped with 2 mol% Er^{3+} and 20 mol% Yb^{3+}, 0.39 mmol of Gd_2O_3, 0.10 mmol of Yb_2O_3, and 0.01 mmol of Er_2O_3 were dissolved in a mixture of 20 mL of acetic acid and 20 mL of water by vigorously stirring at 135 °C under reflux until the mixture became clear. The formed lanthanide acetates ($Ln(OAc)_3$) were extracted by removing the solvents and drying the powder using a rotary evaporator under vacuum at 60 °C. The obtained white powder was used without further modification as the Ln^{3+} precursors. Alternatively, for single doping with 2 mol% Tb^{3+}, 0.48 mmol of Gd_2O_3 and 0.01 mmol of Tb_2O_3 were dissolved in a mixture of 20 mL of acetic acid and 20 mL of water. For co-doping with 20 mol% Yb^{3+} and 2 mol% Tb^{3+}, 0.39 mmol Gd_2O_3, 0.10 mmol Yb_2O_3 and 0.01 mmol Tb_2O_3 were dissolved in the same solvent mixture. The precursors were dried following the same procedure as described above.

Subsequently, 152.2 mg (0.5 mmol) or 304.5 mg (1.0 mmol) of NaOA was added to the flask that contained the dried $Ln(OAc)_3$, yielding a Na-to-Ln molar ratio of 0.5 : 1 and 1 : 1, respectively, together with 1.6 mL of OA (5 mmol), 20.8 mL of ODE (65 mmol), and 11.1 mL of OAm (34 mmol). Previous reports noted that the addition of NaOA to the synthesis is highly beneficial for the particle formation, whereas an alkali-stabilized oleate mesophase acts as a template for nanoparticle nucleation and growth, although Na is not becoming part of the final crystal structure.[27] In fact, under microwave conditions, no solid product could be isolated in the absence of NaOA (Na-to-Ln ratio of 0 : 1). The mixture was degassed under vacuum at 110 °C for 1 h, before adding sulphur, followed by a gas exchange by applying vacuum briefly and flushing with nitrogen three times (note: applying vacuum for too long risks the sublimation of sulphur, reducing its content in the reaction mixture below the set-value; during this step, vacuum was typically applied for a few seconds). To assess the influence of the Ln-to-S ratio, various amounts of sulphur were added, namely 0.5, 1, 2, 4, 8 or 15 mmol, resulting in Ln-to-S molar ratios in the reaction mixture of 1 : 0.5, 1 : 1, 1 : 2, 1 : 4, 1 : 8, and 1 : 15 respectively. Note that, throughout this manuscript, when mentioning Na-to-Ln and Ln-to-S ratios, Ln always refers to the overall amount of Ln^{3+} ions, *i.e.*, the total amount of Gd^{3+} host and Ln^{3+} dopant ions.

The content of the flask was equally distributed between three 35 mL microwave glass vessels using a pre-heated glass syringe, allowing for the synthesis of three batches of NPs. To each vessel a stir bar was added before it was sealed with a Teflon cap and transferred to a CEM Discover SP microwave reactor. In a typical procedure, the reaction mixture was heated as quickly as possible to the reaction temperature of 290 °C. Alternatively, reaction temperatures of 270, 280, and 300 °C were applied (time to reach the maximum temperature of 300 °C: *ca.* 10 min). Once the reaction temperature was reached, it was kept for 10 to 20 min under moderate stirring to allow for NP growth. Following cooling to 25 °C, the reaction mixture containing the NPs was transferred to a 50 mL centrifugation tube, and the NPs were precipitated by adding an equal amount of ethanol, followed by an additional washing step with hexane and ethanol. It should be noted that a second crystalline phase, *i.e.* $NaGdO_2$, could be formed as a by-product (Fig. S1). To remove $NaGdO_2$ and other potential by-products, the particles were further washed with an ethanol/water mixture and once again with ethanol, before being redispersed in toluene for storage and characterization. An overview of all reaction parameters and the respective outcomes is provided in Tables S1–S3 of the SI.

Characterization techniques

The crystalline phase of the obtained materials was determined by powder X-ray diffraction (XRD) analysis using either a Bruker D8 Endeavor (Cu Kα, λ = 1.5401 Å) operating at 44 kV and 40 mA (step size 0.02°, scan speed 0.5° min^{-1}, 30 rev min^{-1}) or a SmartLab Rigaku diffractometer (Rigaku, Tokyo, Japan) operating at 40 kV and 30 mA, equipped with a rotating anode of Cu Kα radiation in grazing incidence mode (0.5°). Therefore, the NPs were drop casted from their toluene dispersion onto a glass substrate. Size, size distribution, and morphology were investigated by transmission electron microscopy (TEM, FEI Tecnai Spirit, FEI Tecnai G2 F20, and JEOL JEM-1400Flash). The samples were dispersed on a Formvar/carbon film supported on a 300-mesh copper TEM grid. Size distributions (mean size ± standard deviation) of the samples were derived from TEM images, using the software Fiji/ImageJ. The thickness of the platelet-like structures was determined by drawing profile lines across vertically stacked particles seen in TEM images using ImageJ and measuring the width of the darkest regions in the intensity profiles, which correspond to the platelet thickness. High resolution TEM (HR-TEM) and energy-dispersive X-ray spectroscopy (EDS) were performed on a JEOL 2100F FEG-TEM operating at 200 kV, equipped with a Gatan K3-IS camera and Oxford Instruments X-Max 80 EDS detector. The Raman spectra were acquired at room temperature using a Thermo Scientific DXR2 micro-Raman equipped with a 633 nm laser at a power of 7 mW. The excitation beam was focused using a 10× or 50× microscope objective, and the Raman signal was collected in backscattering geometry through a 50 μm confocal pinhole aperture, with a variable acquisition time depending on the analysed sample and an estimated spectral resolution of *ca.* 1 cm^{-1}. The Raman spectra were corrected for both the fluorescence and the Rayleigh scattering of each sample. Unless noted otherwise, steady-state photoluminescence properties of the NPs were determined using a highly concentrated particle dispersion (>20 mg mL^{-1} in toluene). Upconversion and NIR emissions were measured in a quartz cuvette (spectral range: 200 to 2500 nm, 1 cm optical path) inserted into a Peltier temperature cuvette holder of a QuantaMaster 8075-21 spectrofluorometer from HORIBA, equipped with double grating emission monochromators, a Hamamatsu red-extended photomultiplier detector R13456 PMT (185 to 980 nm) and a liquid nitrogen cooled InAs detector (1000 to 3450 nm).

The continuous NIR excitation was performed using a 980 nm continuous-wave laser diode (power density: 33.3 W cm^{-2}). UV excitation was performed using an ozone-free PowerArc energy xenon lamp with 72 W. The excitation spectra were corrected for the response of the excitation monochromators and the lamp intensity using a silicon diode reference signal. Emission spectra were corrected for the instrument specific response and the wavelength dependant detection sensitivity of the used detectors using custom, pre-recorded correction files from the manufacturer.

XEOL emission spectra of Tb^{3+}-doped nanostructures were recorded using a custom-made system for radioluminescence spectroscopy.[39] The nanostructures were drop-casted out of their dispersions onto a metallic plate, which was inserted into the chamber. A compact X-ray tube (Magnum 50 kV, 50 μA, TUB00050-W01 - Moxtek Inc.) with a Tungsten target was used as irradiation source. The emission was detected using an optical fibre (QP1000-2-UV/VIS) coupled to a spectrometer (QE65000), both from Ocean Optics. Integration times of 60 s were used. At least three scans were recorded per sample, and the obtained spectra were averaged for final representation.

Results and discussion

Microwave-assisted synthesis of $Gd_2O_2S:Er^{3+}/Yb^{3+}$ nano-triangles

Gd_2O_2S nanostructures co-doped with 20 mol% Yb^{3+} and 2 mol% Er^{3+} to endow the material with upconverting and NIR emitting properties were successfully synthesized using a microwave-assisted method (Fig. 1A and B). Herein, subjecting lanthanide acetates, elemental sulphur, and NaOA as precursors in a mixture of high-boiling point solvents ODE, OA, and OAm to microwave-induced heating at 290 °C for 20 min yielded $Gd_2O_2S:Er^{3+}/Yb^{3+}$ in a triangular morphology (nano-triangles). Based on transmission electron micrographs, the average size of the triangular platelets (tip to edge) was determined as 52 ± 11 nm (Fig. 1B). The self-arrangement of these platelets into stacks allows to estimate their thickness, being in the range of only a few nanometres (*ca.* 3–4 nm, Fig. S2A). High-resolution TEM images of the nano-triangles are shown in Fig. S3. The CrysTBox package was used to measure d-spacings, which resulted in 0.333 nm and 0.193 nm, respectively, compared to expected d-spacings of 0.334 nm for the (100) plane and 0.193 nm for the (110) plane of Gd_2O_2S.[40–42] While Ln_2O_2S is known for its ability to crystallize in various morphologies, including nanoplatelets, to the best of our knowledge, this is not only the first reported microwave-assisted synthesis of Ln_2O_2S NPs but also the first observation of homogenous, colloidal nano-triangles. For the synthesis of the nano-triangles shown in Fig. 1, a Ln-to-S ratio of 1 : 1 and a Na-to-Ln ratio of 0.5 : 1 were used. Indeed, it was found that both ratios play a crucial role when it comes to the control over morphology and crystalline phase purity (*vide supra*). XRD analysis confirmed the crystalline phase of Gd_2O_2S (Fig. 1C), with deviations attributed to the content of smaller Yb^{3+} and Er^{3+} ions replacing some of the Gd^{3+} ions, causing a minor shift of the reflections to higher 2θ values. Similar to other reported two-dimensional materials,[4,27,43] certain diffraction peaks expected for bulk Gd_2O_2S were absent in the XRD pattern, and the intensities also differed from those in the reference pattern. Fast Fourier transform (FFT) analysis and resulting *d*-spacing (*vide infra*) provided further evidence for the formation of crystalline Gd_2O_2S (Fig. S3).

Influence of the Ln-to-S ratio on morphology and phase

Ion ratio and precursor concentration are parameters that are well-known to affect materials formation when it comes to the synthesis of other lanthanide-based materials, such as phase-pure $MLnF_4$ NPs (M = Na, Li), in both conventional and microwave-assisted thermal decomposition routes.[37,44,45] We previously reported that different Ln^{3+}-to-Na^+ ratios allow for the phase-selective formation of cubic and hexagonal $NaLnF_4$ NPs under microwave irradiation.[37] This was ascribed to two important aspects: (i) the effect of the ion ratio itself on phase formation, Na^+ in excess favouring the hexagonal phase, and (ii) the enhanced capability of the ion-enriched reaction mixture to absorb microwave energy (OA/ODE/OAm alone being rather poor microwave absorbers).[32,46] To elucidate any potential effect of

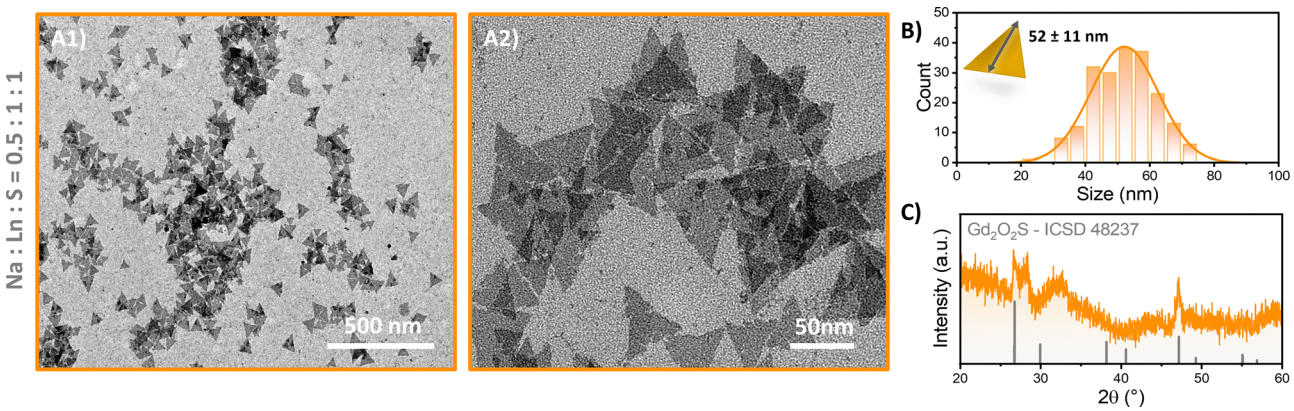

Fig. 1 (A) Low (1) and higher (2) magnification TEM images of triangular shaped $Gd_2O_2S:Er^{3+}/Yb^{3+}$ nanoparticles (nano-triangles) obtained by using a Na-to-Ln-to-S ratio of 0.5 : 1 : 1. Reaction temperature: 290 °C, reaction time: 20 min. (B) Size distribution and average size ± standard deviation for the nano-triangles shown in (A). (C) XRD pattern of the nano-triangles. Reference: Gd_2O_2S, ICSD 48237.

the amount of sulphur in the reaction mixture on the microwave-assisted formation of Gd_2O_2S:Er^{3+}/Yb^{3+} nanostructures, the Ln-to-S ratio was varied between 1 : 0.5 (stoichiometric ratio) and 1 : 15 (30-times excess of sulphur), while keeping the amount of sodium added *via* NaOA constant at a Na-to-Ln ratio of 0.5 : 1.

Morphology and crystalline phase. Interestingly, a drastic change in the shape of the particles was observed as a function of sulphur content (Fig. 2). As presented above, a Ln-to-S ratio of 1 : 1 resulted in the formation of nano-triangles (Fig. 1 and 2B). While triangle-like particles were also observed upon the addition of a stoichiometric amount of sulphur (Ln-to-S ratio of 1 : 0.5), the TEM image in Fig. 2A unveils small nanoparticles of *ca.* 6 nm in diameter as a secondary morphology (Fig. S4). Moreover, the triangular platelets (*ca.* 40 nm in size) were poorly developed, providing evidence for the significant role of the sulphur concentration for nano-triangle formation. The presence of more sulphur in the reaction mixture (Ln-to-S = 1 : 2) resulted in heterogeneous agglomerates of quasi-spherical nanostructures alongside nano-triangles of *ca.* 50 nm in size (Fig. 2C and Fig. S6). Upon further increase of the Ln-to-S to 1 : 4, the growth of nano-triangles was suppressed, and the formation of spherical agglomerations built by smaller NPs was fostered, which resembled a raspberry-like morphology (Fig. 2D and Fig. S7). TEM analysis indicated that these agglomerated nanostructures might also contain irregularly shaped, thin platelets (*ca.* 2 nm in thickness), as those shown in Fig. S2B. Up to a Ln-to-S ratio of 1 : 4, XRD analysis confirmed the formation of Gd_2O_2S as sole crystalline phase, irrespective of the amount of sulphur added (Fig. 2G). Herein, upon increase of the Ln-to-S ratio, the XRD patterns were characterized by increasingly pronounced reflections indicating the formation of more crystalline material. This result is plausible considering that the competing processes of Ln_2O_3 and Ln_2O_2S formation are heavily influenced by the sulphur amount available in the reaction mixture.[47,48] Conversely, when sulphur was added in a 1 : 8 or 1 : 15 ratio (Fig. 2E and F and Fig. S8 and S9), flower-like NPs similar to those known in the literature were formed (note that the terms "nano-berries" and "nano-flowers" were chosen to reflect the distinct structural characteristics observed in these samples; while the nano-berries represented more heterogenous agglomerates, the nano-flowers exhibited a well-defined platelet-like morphology).[4,7] The overall size of the nano-flowers was *ca.* 30 and 50 nm, for 1 : 8 and 1 : 15 Ln-to-S ratios, respectively. Individual "petals" of *ca.* 10 nm could be identified when the ratio was 1 : 8. At this point, additional XRD reflections at 21.7° and 23.8° 2θ values were found in the XRD patterns. Interestingly, these observed reflections (Fig. 2G and Fig. S10) are consistent with stearic hydrazide and polymeric species, such as carnauba wax, suggesting the formation of similar structures, potentially driven by unreacted sulphur precursors and inverse vulcanization of OA/OAm at elevated temperatures.[49–51] Possibly, the formation of these long-chained species further impacted the morphology of the nanoparticles as observed when

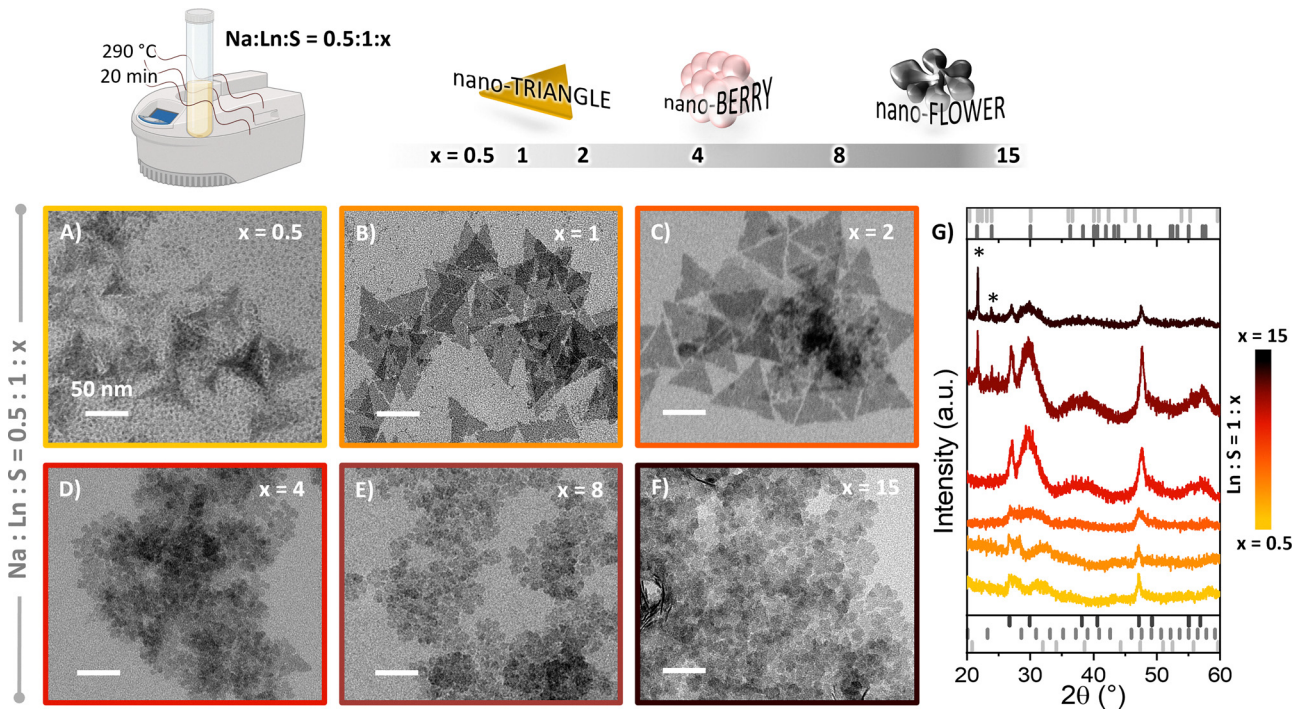

Fig. 2 TEM images of the nanomaterials obtained under microwave irradiation at 290 °C for 20 min as a function of the Ln-to-S ratio, *i.e.*, (A) 1 : 0.5, (B) 1 : 1, (C) 1 : 2, (D) 1 : 4, (E) 1 : 8, and (F) 1 : 15. All scale bars are 50 nm. The Na-to-Ln ratio was 0.5 : 1 for all samples. Additional TEM images and size distributions are provided in Fig. S4 to S9. The respective XRD patterns of the nanomaterials are shown in (G). References (bottom): Gd_2O_2S (dark grey, ICSD 48237), Gd_2O_3 (grey ICSD 48238), and $NaGdO_2$ (light grey, ICSD 97542). Additional crystalline phases, marked with an asterisk (*), were observed for the most extreme conditions with Ln-to-S ratios of 1 : 8 and 1 : 15. These reflections may correspond to either carnauba wax or stearic hydrazide. References (top): carnauba wax (dark grey, PDF 00-072-1406), stearic hydrazide (light grey, PDF 00-034-1786). See also Fig. S10.

increasing the sulphur amount, including a more pronounced tendency for agglomeration as observed in case of nano-flowers. Lei *et al.* previously reported the formation of *ca.* 40 nm sized nanodisks as well as smaller, flower-like Ln_2O_2S NPs by thermal decomposition, whereas lower amounts of sulphur favoured the formation of larger disks.[7] The two-dimensional growth of Gd_2O_2S can be ascribed to the capping of the (001) facets of Gd_2O_2S by surfactants, such as oleate, favouring growth in the {100} and {110} planes, as also evidenced by high-resolution TEM analysis (Fig. S3).[24,52] Based on TEM analysis of the samples obtained at an increasing Ln-to-S ratio, an excessive amount of sulphur seemed to undermine such effective protection of the (001) facets. Consequently, (i) the formation of two-dimensional, triangular nanostructures and (ii) the dispersibility in the solvent of the Ln_2O_2S nanostructures was hampered leading to the formation of agglomerates of smaller NPs. Though, careful inspection of TEM images recorded on samples obtained at Ln-to-S ratios larger than 1 : 4 unveiled the formation of two-dimensional flower-like particles that tend to agglomerate, at times in form of stacks (as indicated by the darker lines in Fig. 2F and Fig. S2, S8, and S9) as previously reported by Larquet *et al.*[27] The estimated thickness of these particles was *ca.* 2.7 nm (Fig. S2C).

Overall, the amount of sulphur plays a critical role in the growth mechanism of Ln_2O_2S, most likely due to the disturbance of the efficient capping of the (001) facets leading to (i) poorer dispersibility and (ii) hampering of the triangular lateral growth in favour of particle formation, including growth into two-dimensional flower-like nanostructures. It is reasonable to note that the formation of polymeric species formed by the hydrophobic tails linked through the double bond of the capping oleate groups and S addition, further impacts the morphology of the nanoparticles as observed when increasing the sulphur amount, including a more pronounced tendency for agglomeration. Additionally, while an excess of sulphur clearly hinders the formation of well-defined triangular structures, the growth process nevertheless requires a sulphur concentration higher than expected based purely on stoichiometric considerations.

Elemental mapping. While XRD indicated the formation of crystalline Gd_2O_2S, the elemental composition and morphology-dependent elemental distribution was further assessed by EDS mapping. Two representative samples were selected, predominantly exhibiting nano-triangular and berry-like morphologies, respectively (Fig. S11A). EDS mapping revealed a homogeneous distribution of Gd, Yb, O, and S across both morphologies (Fig. S11B and C). The qualitative analysis showed good agreement with the nominal Gd-to-Yb ratio (20 mol% Yb). However, sulphur appeared in lower-than-expected concentrations, particularly in the nano-triangular structures, with EDS-derived S-to-Gd ratios of less than 0.1 and 0.3 for nano-triangles and nano-berries, respectively. Such deviations are not uncommon and have been previously reported, especially in platelet-like morphologies that preferentially expose Gd-rich surfaces.[4,27] The determination of oxygen content *via* EDS measurements does not align with the expected values for Gd_2O_2S, and a significantly higher oxygen signal was observed in the analysis, which can be attributed to the used Formvar-coated grids during sample preparation. These grids inherently contribute to the detected oxygen signal, leading to an overestimation of the oxygen content in the sample. In addition, it is known that the sample holder also can contribute to the oxygen signal in EDS measurements.[53] We emphasize that EDS is used here as a qualitative tool to assess elemental distribution rather than to confirm stoichiometry or phase purity. Due to the known limitations of EDS, particularly for light elements such as oxygen and its surface sensitivity, the quantitative interpretation of atomic percentages should be approached with caution. Phase purity is instead supported by XRD and Raman spectroscopy (*vide supra*), which together provide complementary and more reliable structural information.

Raman spectroscopy. To gain additional insight into the chemical and structural composition of the obtained nanostructures, Raman spectroscopy was performed. Special attention was paid to potential effects of the Ln-to-S ratio, which strongly influenced the morphology of the formed Ln_2O_2S nanostructures. Room temperature Raman spectra recorded on samples obtained at different Ln-to-S ratios ranging from 1 : 0.5 to 1 : 15 (with a constant Na-to-Ln ratio of 0.5 : 1) are displayed in Fig. 3A and Fig. S12A. From a comparison with the Raman spectra of pure Na-oleate and OAm (Fig. S12B), the Raman bands in the region between 1000 and 4000 cm^{-1} for all the samples are due to the vibrations typical of the organic backbone of the capping agents, *i.e.* oleate and oleylamine molecules. Interestingly, from Fig. S12A it can be noted that the overall intensity of the Raman band around 1660 cm^{-1} decreases on increasing the S amount in the starting mixture. This band is attributed to C=C stretching vibrational mode, typical of the oleic organic tail.[54] The decrease of the Raman intensity for this band suggests that the C=C double bond reacts with the elemental S in the reaction mixture, forming a C–S bond as also evidenced by other authors.[50,55] This behaviour

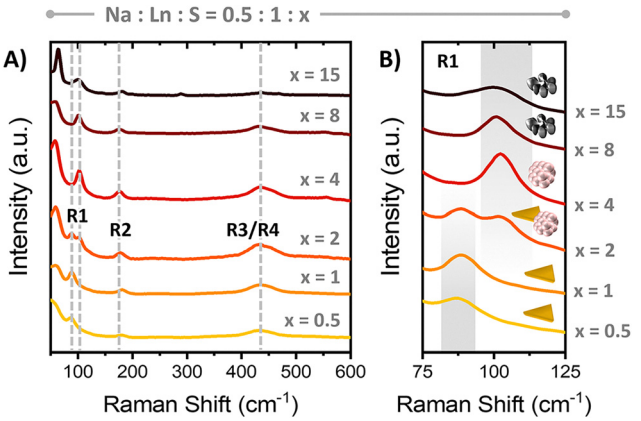

Fig. 3 (A) Raman spectra for $Gd_2O_2S:Er^{3+}/Yb^{3+}$ nanostructures at room temperature, obtained at a different Ln-to-S ratios of 1 : 0.5, 1 : 1, 1 : 2, 1 : 4, 1 : 8, and 1 : 15. The Na-to-Ln ratio was kept constant at 0.5 : 1. Microwave reaction conditions: T = 290 °C, t = 20 min. Panel (B) displays the magnified spectral region of band R1. Extended range Raman spectra are provided in Fig. S12.

is further corroborated by the increase of the broad bands in the 700–800 cm^{-1} range, which could be attributed to C–S stretching vibrations.[56] Moreover, four quite broad Raman bands were observed at Raman shift lower than 500 cm^{-1}, in good agreement with those reported by Yokono *et al.* for bulk Gd_2O_2S phosphors.[57] According to the authors, these four Raman lines, denoted as R_1, R_2, R_3, and R_4 (Fig. 3A), are assigned to low-frequency E_g, A_{1g}, and high-frequency E_g, and A_{1g} vibrational modes, respectively, typical of the gadolinium oxysulfide crystal lattice. Hence, the Raman spectra point to further evidence for the successful formation of Gd_2O_2S by microwave-assisted synthesis.[15,57]

The average Raman shifts for the R_2 (around 190 cm^{-1}) and the R_3/R_4 bands (around 440 cm^{-1}) are in perfect agreement with those found in the literature. However, the R_3 and R_4 bands appear merged, reasonably due to the nanosized nature of the samples. Interestingly, the R_1 Raman band strongly depends on the amount of sulphur in the reaction mixture and hence, the morphology of the nanostructures (Fig. 3B). For Ln-to-S ratios of 1 : 4, 1 : 8, and 1 : 15, leading to nano-berries and -flowers (Fig. 2D–F), the R_1 band is centred around 103 cm^{-1}, slightly lower than the value found for undoped Gd_2O_2S (107 cm^{-1}) as reported by Yokono *et al.*[57] This small redshift of the Raman band could be explained by the presence of high amounts of heavier Yb^{3+} and Er^{3+} ions in the present samples with respect to the Gd^{3+} ions, resulting in a lower vibrational mode energy.[57]

Upon synthesis of Gd_2O_2S:Er^{3+}/Yb^{3+} in the presence of less sulphur (Ln-to-S of 1 : 0.5 and 1 : 1), nano-triangles were obtained (Fig. 2A and B). For these nano-triangles, the rise of a new band at lower Raman shift, around 90 cm^{-1}, was observed, while the band at 103 cm^{-1} correspondingly disappeared with the two most pronounced sulphur-deficient compositions of the nanostructures (x = 0.5 and 1, Fig. 3B). While Raman bands below 100 cm^{-1} were reported for Gd_2O_3,[58] the Raman spectra recorded on the sulphur deficient samples did not evidence cubic nor monoclinic Gd_2O_3 phases, in agreement with XRD patterns recorded on these samples, which lack the characteristic reflections in the 20 to 25° 2θ range (Fig. 2G). Therefore, at this point, we hypothesize that the observed band around 90 cm^{-1} might be caused by a decrease in the phonon energy of the host crystal due to the platelet-like structure of the nano-triangles, which exhibited only a few nanometres in thickness as seen in TEM. This was further corroborated by the results of X-ray diffractometry, characterized by missing reflections in the XRD patterns due to the nanostructures' anisotropy and critical dimensions on the order of a few nanometres.[59] It could be reasonable to hypothesize that the oleate moieties coordinating the surface through the oxygens of the carboxylic group could lengthen the bond of gadolinium with the other lattice ions to some extent and decrease the energy of low-energy lattice vibrational modes.

The Raman spectrum obtained at a 1 : 2 Ln-to-S ratio is particularly interesting, showing both the bands around 90 and 103 cm^{-1} (Fig. 3B). In this case, indeed, TEM analysis unveiled a mixture of nano-triangles and berry-like nanostructures.

Overall, the results of complementary XRD and EDS analysis as well as Raman spectroscopy provide clear evidence for the formation of Ln_2O_2S nanocrystals *via* microwave-assisted synthesis.

Proposed growth mechanism

Noteworthy, by choosing a microwave-assisted approach, crystalline, colloidal Gd_2O_2S:Er^{3+}/Yb^{3+} nano-triangles could be achieved within significantly shorter reaction time (20 min) than possible by more conventional approaches. Solid-state reactions, solvothermal synthesis, and thermal decomposition under convectional heating typically require reaction times that range from a few hours to days. For instance, Yorov *et al.* observed a morphological change from flower-like Gd_2O_2S:Tb^{3+} NPs to nanoplatelets when prolonging the reaction time of the thermal decomposition from 4 to 30 h.[4] In contrast, we observed formation of triangular platelets within 20 min. We previously reported the microwave-induced rapid formation of specific crystalline phases and morphologies for materials that belong to the alkali metal lanthanide tetrafluoride family, $MLnF_4$ (M = Na, Li). For instance, a fast cubic-to-hexagonal phase transformation at the sub-minute-scale was observed for $NaGdF_4$:Ln^{3+} NPs.[37] When seeking $LiYF_4$:Ln^{3+}, micron-sized particles of distinct orthorhombic morphology were obtained within 10 min.[60] Beyond $MLnF_4$, tuneable morphologies of $NaMnF_3$, *i.e.*, rods, ribbons, and plates, were obtained upon microwave-assisted decomposition of sodium and manganese trifluoroacetate precursors in varying Na^+-to-Mn^{2+} ratios within 20 min.[61] In all cases, microwave conditions favoured the rapid morphological and/or phase transformation, allowing for more rapid materials formation than conventionally observed.

Effect of reaction time. To gain further insight into the formation of Ln_2O_2S under microwave irradiation and to propose a growth mechanism, the reaction time was systematically changed, while keeping all other parameters constant. First, the time-dependent formation of nano-triangles as the most interesting among the obtained morphologies was assessed. Therefore, the reaction time was gradually shortened from 20 to 15 to 10 min, while the Na-to-Ln-to-S ratio was set to 0.5 : 1 : 1. The reaction temperature was 290 °C. TEM analysis unveiled that indeed a reaction time of 20 min was required to yield homogeneous nano-triangles (Fig. 4). A shortening of the microwave-irradiation resulted in heterogeneous size and morphology distributions. As such, after 10 min, small NPs of heterogenous size and morphology were formed, while additional nanostructures were observed that pointed already towards the formation of triangular platelets (Fig. 4A). Prolonging the reaction time to 15 min resulted in fewer quasi-spherical NPs and more pronounced triangular structures, which resembled three-pointed stars (Fig. 4B) and grew to *ca.* 35 nm in size (size distribution histograms are provided in Fig. S13). Ultimately, upon continuous heat treatment the intermediate spherical morphology disappeared, and the three-pointed star-like NPs grew into well-defined nano-triangles of *ca.* 50 nm (Fig. 4C). While the morphology changed significantly as a function of reaction time, XRD analysis indicated that the crystallization of Ln_2O_2S

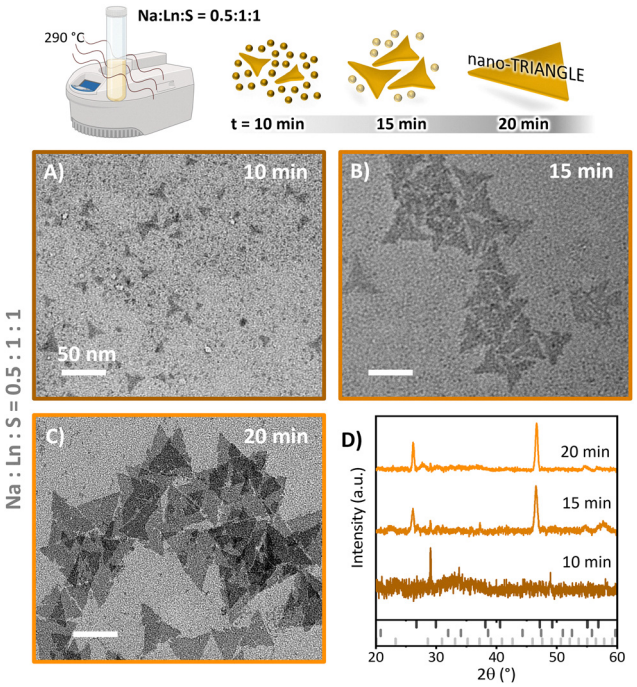

Fig. 4 TEM images of materials obtained under microwave irradiation at 290 °C for (A) 10 min, (B) 15 min, and (C) 20 min. The Na-to-Ln-to-S ratio was kept constant at 0.5 : 1 : 1. The scale bar given in panel (A) applies to all TEM images. (D) Corresponding XRD patterns. References: Gd_2O_2S (dark grey, ICSD 48237), $NaGdO_2$ (grey, ICSD 97542), and Gd_2O_3 (light grey, ICSD 48238).

started even at the shortest reaction time (Fig. 4D). Though, longer reaction times were required for higher crystallinity, as evidenced by the more pronounced characteristic reflections in the XRD patterns recorded on samples obtained after 15 and 20 min of microwave treatment. Hence, the growth of small NPs, acting as nuclei or seeds,[7] as well as the formation of fragmented nano-triangles was identified as intermediate steps towards the formation of well-defined nano-triangles. Herein, the nano-triangles underwent lateral growth, leading to a "straightening" of the triangles' edges. As mentioned above, the lateral growth can be ascribed to the strong bonding between Gd^{3+} cations and oleate anions on the (001) facets of Gd_2O_2S, which results in lateral growth of the nanoplatelets in the {100} and {110} planes through a time-dependent Ostwald-ripening process.[4,24,52,62] Overall, as reported by Yorov *et al.*, time was identified as a key aspect in the formation of homogenous Gd_2O_2S nanoplatelets, whereas microwave-induced heating significantly shortened the kinetically controlled growth process. Yet, while Yorov *et al.* observed a distinct morphological evolution of well-defined morphologies, the rapid nucleation and growth processes under microwave conditions did not allow for the time-controlled synthesis of selective, pure morphologies beyond nano-triangles.

Effect of Ln-to-S ratio. While adjustment of the duration of the microwave treatment alone did not offer access to Ln_2O_2S of various, distinct morphologies, different Ln-to-S ratios selectively yielded nano-triangles, -berries, and -flowers (*vide infra*) after 20 min. To better understand the formation of these Ln_2O_2S nanostructures, we shortened the reaction time, while also studying the effect of the Ln-to-S ratio. Therefore, the synthesis was conducted for 10 to 20 min using Ln-to-S ratios spanning a wide range from 1 : 0.5 to 1 : 15 (with a constant Na-to-Ln ratio of 0.5 : 1). TEM analysis unveiled that a larger amount of sulphur in the reaction mixture led to the faster formation of the characteristic morphological features (Fig. S14). For instance, the formation of nano-triangles was observed after 10 min at a Ln-to-S ratio of 1 : 2, whereas the formation process was slower in case of ratios of 1 : 0.5 and 1 : 1 (Fig. S14A–C). Particularly at a stoichiometric Ln-to-S ratio of 1 : 0.5, a reaction time of 20 min was not sufficient to completely transform the small, quasi-spherical NPs into nano-triangles (Fig. S14A). Moreover, for ratios ranging from 1 : 0.5 to 1 : 2, lateral growth and Ostwald-ripening of the nano-triangles could be observed with increasing reaction time. Conversely, at high Ln-to-S ratios of 1 : 8 and 1 : 15, nano-flowers were formed after 10 min, a morphology that remained unchanged upon longer microwave treatment. Moreover, the size of the nano-flowers barely changed as a function of reaction time, considering standard deviations (Fig. S14E and F).

A Ln-to-S ratio of 1 : 4 was deemed particularly interesting, as it represented a borderline between the conditions that resulted in nano-triangles and those that yielded nano-flowers. TEM images shown in Fig. 5A unveiled a mixture of morphologies, including nano-triangles, irregular shapes, and first assemblies into nano-berries. Compared to the triangles obtained at a lower Ln-to-S ratio of 1 : 2 (Fig. S14C1, *ca.* 30 nm), fewer triangles of smaller size (*ca.* 20 nm, Fig. 5B) were obtained at a ratio of 1 : 4. These observations provide additional insight into the materials formation mechanism, *i.e.*, evidence that a critical sulphur content is required for the growth of well-formed nano-triangles within short reaction times. At lower ratios (Ln-to-S $<$ 1 : 2), quasi-spherical NPs made a large portion of the obtained material. Above a critical amount, *i.e.*, at Ln-to-S $>$ 1 : 2, limited formation of nano-triangles was observed in favour of heterogeneous platelets, while assembly into agglomerated nano-berries started (Fig. 5C). Interestingly, this formation of nano-berries was not only triggered by providing larger amounts of sulphur. It could also be induced by prolongation of the reaction time from 10 to 15 and 20 min, respectively, while keeping the Ln-to-S ratio at 1 : 4 (Fig. S14D2/3). Of note, the size of the obtained nano-berries did not follow a clear trend with reaction time (Fig. S14D4). Lastly, careful inspection of TEM images recorded on samples obtained after 20 min at a 1 : 4 ratio (Fig. S14D3) indicated the presence of particles that resembled two-dimensional flower-like platelets, like those the formation of which became prominent at higher Ln-to-S ratios (*vide infra*), a trend that was fostered upon further prolongation of the reaction time to 30 min (Fig. S15).

In agreement with TEM analysis, XRD patterns of samples obtained after 15 min of microwave treatment unveiled more pronounced reflections compared to those on samples irradiated for only 10 min (Fig. S16). This time dependence of the

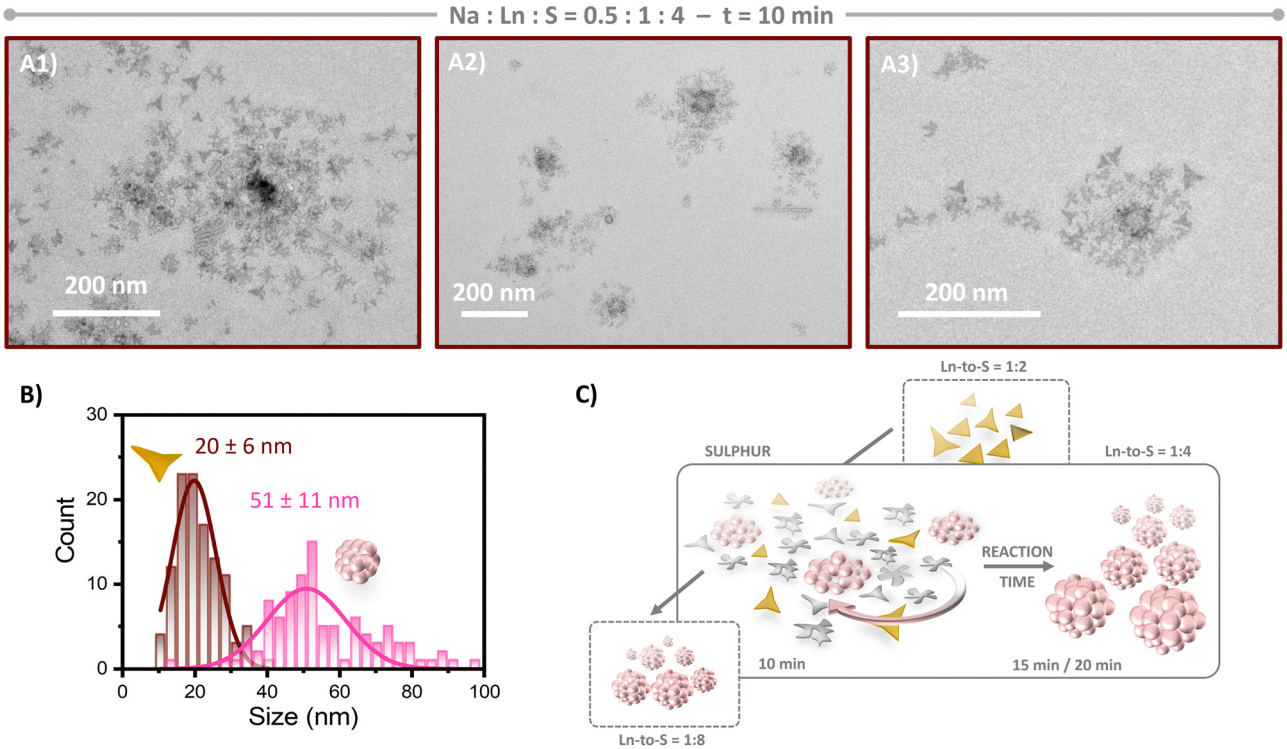

Fig. 5 (A) TEM images of different magnification showing nanomaterials obtained under microwave irradiation at 290 °C for 10 min using a Ln-to-S ratio of 1 : 4. The Na-to-Ln ratio was 0.5 : 1. (B) Size distribution histograms including average size ± standard deviation for nano-triangles and berry-like structures. (C) Scheme representing the proposed morphology evolution as a function of sulphur content and reaction time.

crystallization process was particularly pronounced for Ln-to-S ratios of up to 1 : 2, as evident from the lack of typical reflections and lower signal-to-noise ratios after shorter reaction time. These observations provided further evidence for a kinetically controlled materials formation.

Effect of Na-to-Ln ratio. Based on the findings described above, reaction time and sulphur content were identified as key parameters with respect to Ln_2O_2S formation under microwave-induced heating. Though, it must be kept in mind that sodium was required as additional ion in the reaction mixture to foster materials formation.[27] To investigate the effect of sodium under microwave conditions, the reactions were further performed at a higher Na-to-Ln ratio, *i.e.*, 1 : 1 (opposed to 0.5 : 1 for all samples discussed above), while keeping all other parameters constant. As shown in Fig. S17A and B, both Ln-to-S ratios of 1 : 0.5 and 1 : 1 led to nano-triangles (Na-to-Ln ratio of 1 : 1). Yet, opposed to the above-described samples, TEM micrographs recorded on samples obtained at a higher sodium content showed thin lamellar arrangements at a Ln-to-S ratio of 1 : 0.5 and 10 min of microwave treatment (Fig. S17A1). These self-assembled structures are proposed to be formed by stacked platelets. As expected, a higher content in sulphur fostered triangle growth at shorter reaction times. Though careful inspection of the TEM images allowed for further insight into materials formation in the presence of more sodium. The TEM image in Fig. S17B1 (Ln-to-S = 1 : 1, 10 min) demonstrates the formation of the nano-triangles by self-assembly of smaller fragments. This resulted in structured edges of the triangles, giving the impression of a Christmas tree-like shape. Upon prolonged heat-treatment, these fragments grew into a complete triangular shape with straight edges (Fig. S17B2 and 3). Such evolution from fragmented into complete triangles was also observed at a Na-to-Ln ratio of 0.5 : 1, though fragmentation was less pronounced, resembling a three-pointed star (Fig. 4A and B). Moreover, a higher sodium content fostered the lateral growth of the nano-triangles to up to *ca.* 70 and 80 nm after 20 min for Ln-to-S ratios of 1 : 0.5 and 1 : 1, respectively. To recall, smaller sized nano-triangles of up to *ca.* 50 nm were obtained for a Na-to-Ln ratio of 0.5 : 1 (Fig. S14A and B). At a Na-to-Ln ratio of 1 : 1 and a Ln-to-S ratio of 1 : 4, berry-like assemblies (*ca.* 72 nm) were formed after 10 min (besides larger, heterogenous agglomerates), while disk-like structures (*ca.* 53 nm) were formed after 15 min (Fig. S17C), which resembled those reported by Yorov *et al.*[4] upon thermal treatment for 4 to 20 h. Hence, lateral growth from fragmented to complete nano-triangles as well as from nano-berries to disk-like structures took place at Ln-to-S ratios of 1 : 1 and 1 : 4, respectively. In both cases, this morphological change of the NPs resulted in the minimization of areas with high curvature. This can be ascribed to Ostwald-ripening processes, which cause atoms to move from areas of high curvature to areas of lower curvature to reduce the surface energy.[4,63]

Lastly, TEM images recorded on samples obtained at a Ln-to-S ratio of 1 : 15 in the presence of higher sodium content showed agglomerations of spherical particles and flower-like structures like those found at the lower Na-to-Ln ratio of 0.5 : 1

(Fig. S17D). In addition, stacks of two-dimensional nanoplatelets could be identified (black lines in, *e.g.*, Fig. S17D2) similar to those reported by Larquet *et al.*[27] Herein, the size of the obtained particles was in the order of 43 to 46 nm, thus, lacking any trend with reaction time.

XRD patterns shown in Fig. S18 confirm the formation of crystalline Ln_2O_2S as a function of reaction time and sulphur content. As seen in case of a Na-to-Ln ratio of 0.5 : 1, also at a ratio of 1 : 1, the crystallinity of the material increased with increasing sulphur content as well as longer reaction time.

Overall, irrespective of the sodium content, nano-triangles, berry-, and flower-like nanostructures were formed depending on the amount of sulphur available in the reaction mixture. However, it should be noted that the structural integrity and purity of the resultant particles was of lower quality at a Na-to-Ln ratio of 1 : 1 opposed to 0.5 : 1. To understand the role of sodium in the reaction mixture, it should be recalled that OA, ODE, and OAm – used as solvents in the reaction – alone are rather poor microwave absorbers.[32,46] In contrast, the enhanced capability of the sodium ion-enriched reaction mixture to absorb microwave energy might explain the observed differences in structure and size as a function of sodium concentration. For instance, we previously reported that a higher sodium content is required for the microwave-assisted synthesis of hexagonal-phase $NaLnF_4$ compared to its cubic counterpart.[37] Similarly, in case of Ln_2O_2S, a higher sodium concentration might provide the system the energy required for faster materials formation. As a consequence, larger particles, particularly nano-triangles, were formed. However, the faster growth kinetics might also be the cause for the increased observation of additional irregular shapes as well as less crisp and more fuzzy nanostructures (*e.g.*, those shown in Fig. S17C1).

Effect of reaction temperature. Finally, to evaluate whether a lower temperature regime would be sufficient for inducing Ln_2O_2S formation at Na-to-Ln-to-S ratios of 1 : 1 : 1 (nano-triangles) and 1 : 1 : 4 (nano-berries), respectively, the reaction temperature was decreased from 290 °C to 280 °C and 270 °C. Yet, no product could be isolated under the investigated microwave conditions. Conversely, increasing the reaction temperature to 300 °C allowed for the isolation of crystalline and phase-pure Ln_2O_2S nano-triangles and -berries already after 10 min of microwave-induced heating (Fig. S19). Particularly, the formation of homogenous and well-defined nano-triangles within such short reaction time was enabled by increase of the reaction temperature, with a few sub-10 nm sized NPs as secondary morphology. In contrast, a reaction time of 290 °C yielded fragmented nano-triangles along with additional heterogenous structures. An elevated temperature also favoured the growth of nano-berries, resulting in crisper nanostructures after shorter reaction time, though, the size of the nano-berries remained unchanged. These findings indicate a growth mechanism that is not only kinetically (*vide infra*) but also thermodynamically controlled.

Optical properties of Er^{3+}/Yb^{3+}-doped Gd_2O_2S nanostructures

Upconverting and NIR emitting $Gd_2O_2S:Er^{3+}/Yb^{3+}$. Er^{3+}/Yb^{3+}-doped Gd_2O_2S nano-triangles, berry-, and flower-like nanostructures dispersed in toluene obtained by microwave-assisted synthesis at 290 °C for 20 min, using a Ln-to-S ratio of 1 : 1, 1 : 4, and 1 : 8, respectively (Na-to-Ln ratio: 0.5 : 1), showed upconversion and NIR emission under 980 nm excitation (Fig. 6A and B). The characteristic upconversion emission peaks in the green and red spectral regions are ascribed to the $^2H_{11/2} \rightarrow {}^4I_{15/2}$ (520 nm), $^4S_{3/2} \rightarrow {}^4I_{15/2}$ (550 nm) and $^4F_{9/2} \rightarrow {}^4I_{15/2}$ (650 nm) Er^{3+} transitions (Fig. 6C). Across all morphologies, the red emission band ($^4F_{9/2} \rightarrow {}^4I_{15/2}$, *ca.* 650 nm) was more intense than the green bands ($^2H_{11/2}/{}^4S_{3/2} \rightarrow {}^4I_{15/2}$, *ca.* 520–550 nm), with a red-to-green (R/G) peak intensity ratio of approximately 2 : 1. This predominance of red emission is commonly attributed to an efficient non-radiative depopulation of the green-emitting levels, which can arise from several parasitic processes. These include surface-related quenching effects, particularly in smaller or highly agglomerated particles, as well as cross-relaxation and energy back-transfer mechanisms between Er^{3+} and Yb^{3+} ions at higher dopant concentrations. Additionally, local lattice distortions or strain, especially in anisotropic morphologies as those investigated herein, may enhance multi-phonon relaxation processes (MPR), further favouring red emission. Moreover, the capping molecules, presenting carboxylate- and amino-groups, have molecular vibrations that can increase the MPR, in particular for the lanthanide ions located on the (large) nanoparticle surface. On the other hand, similar red-dominant emission behaviour has been reported for Er^{3+}/Yb^{3+}-doped Gd_2O_2S systems and is consistent with the host's relatively low phonon energy, which supports upconversion but does not entirely suppress non-radiative losses.[64] The NIR emission at *ca.* 1500 nm stems from the Er^{3+} $^4I_{13/2} \rightarrow {}^4I_{15/2}$ transition. The photoluminescence signals of all three samples were clearly detectable with favourable signal-to-noise ratios, especially considering the challenging morphologies involved, namely thin triangular platelets (less than 3 nm in thickness), berry-like nanoparticle agglomerates, and flower-shaped 2-dimensional nanostructures (less than 3 nm in thickness), all of which are characterized by a high surface-to-volume ratio that typically promotes surface-related quenching effects. Irrespective of the morphology of the investigated $Gd_2O_2S:Er^{3+}/Yb^{3+}$ nanostructures, the Er^{3+} NIR emission exhibited three sub-peaks, which are the result of Stark splitting (well-defined Stark splitting was further observed for nano-triangles in powder form, Fig. S20). Close inspection of the spectra shown in Fig. 6B unveiled that the NIR emission peaked at 1543 nm for nano-triangles, while the maximum emission centred at 1550 nm for berry- as well as flower-like nanostructures. In addition, the spectrum recorded on the nano-triangles exhibited minor peak broadening compared to the other two nanostructures. The platelet-like, thin morphology of the nano-triangles can affect the crystal lattice, as evidenced by XRD and Raman data, which in turn might cause this slight blue-shift of the maximum emission and peak broadening.

Tb^{3+}-doped Gd_2O_2S nanostructures

Synthesis. To demonstrate the versatility of the developed microwave-assisted approach regarding the synthesis of Ln_2O_2S

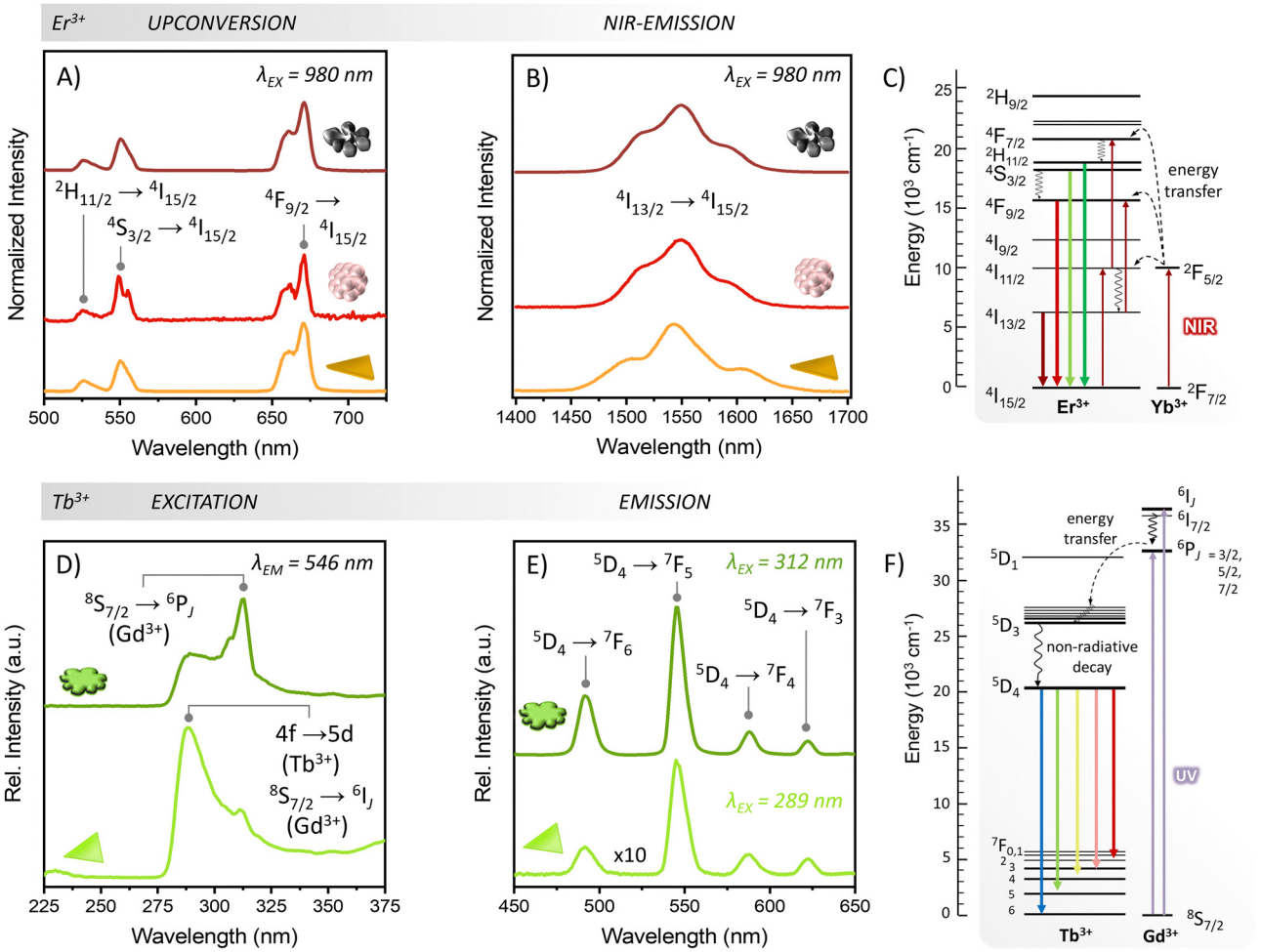

Fig. 6 (A) Upconversion (UC) and (B) NIR spectra of Er^{3+} (2 mol%) and Yb^{3+} (20 mol%) co-doped Gd_2O_2S nano-triangles, berry-, and flower-like nanostructures dispersed in toluene upon excitation with 980 nm (laser power density: UC – 33.3 W cm^{-2}, NIR – 34.6 W cm^{-2}). Reaction conditions for sample preparation: microwave irradiation at 290 °C for 20 min; Na–Ln ratio: 0.5 : 1, Ln–S ratio: 1 : 1, 1 : 4, and 1 : 8 for nano-triangles, berries, and flowers, respectively. (C) Yb^{3+} and Er^{3+} energy levels highlighting the emissions observed at the spectra shown in panels (A) and (B). (D) Excitation spectra of Tb^{3+} (2 mol%) and Yb^{3+} (20 mol%) co-doped Gd_2O_2S nano-triangles as well as Tb^{3+} (2 mol%) doped Gd_2O_2S flower-like nanostructures monitoring the 546 nm emission of Tb^{3+}. (E) Emission spectra of Tb^{3+} (2 mol%) and Yb^{3+} (20 mol%) co-doped Gd_2O_2S nano-triangles as well as Tb^{3+} (2 mol%) doped Gd_2O_2S flower-like nanostructures under 289 nm and 312 nm excitation, respectively. Reaction conditions for sample preparation: microwave irradiation at 290 °C for 20 min; Na–Ln ratio: 1 : 1, Ln–S ratio: 1 : 0.5 and 1 : 8 for nano-triangles and flowers, respectively. (F) Tb^{3+} and Gd^{3+} energy levels highlighting the emissions observed at the spectra shown in panel (E).

nanostructures, we synthesized Tb^{3+}-doped (2 mol%) Gd_2O_2S flower-like structures as well as Gd_2O_2S nano-triangles co-doped with Tb^{3+} and Yb^{3+} (2 mol% and 20 mol%, respectively) to harness the UV-excited green emission of the Tb^{3+} ion. The same reaction conditions were chosen as for Er^{3+}/Yb^{3+}-doped samples, *i.e.*, microwave irradiation at 290 °C for 20 min. A Ln-to-Na ratio of 1 : 1 was chosen, and the amount of sulphur was adjusted to obtain nano-triangles (Ln-to-S ratio of 1 : 0.5) as well as flower-like nanostructures (Ln-to-S ratio of 1 : 8). As a result, the morphology and size of the Tb^{3+}-based structures were comparable to those of the Er^{3+}-doped analogues (Fig. S21). It should be noted however, that Yb^{3+} played a key role in the formation of homogeneous nano-triangles. While the effect of the lanthanide ion on, *e.g.*, the crystallization of $NaLnF_4$ is well-known,[44,65,66] future studies will have to be performed to unveil trends and underlaying mechanisms in the microwave-induced formation of Ln_2O_2S nanostructures as a function of the chosen lanthanide ion.

Optical properties. Excitation and emission spectra recorded for Tb^{3+}- and Tb^{3+}/Yb^{3+}-doped nano-triangles and flower-like nanostructures are given in Fig. 6D and E, respectively. The corresponding energy level diagram is shown in Fig. 6F. Characteristic excitation bands of the Gd^{3+} ion indicate a possible indirect excitation of Tb^{3+} through the Gd^{3+} ions of the host matrix (Fig. 6D).[67] Interestingly, the most efficient excitation was found to depend on the nanostructures' morphology. For nano-flowers, the most intense excitation peak was at 312 nm, corresponding to the Gd^{3+} ^6P_J levels. For nano-triangles, a shorter excitation wavelength, namely 289 nm, corresponding to the Gd^{3+} ^6I_J levels, was found to be more efficient. Besides Gd^{3+} f–f transitions, this band at 298 nm could also have contribution from the band edge of the Gd_2O_2S host

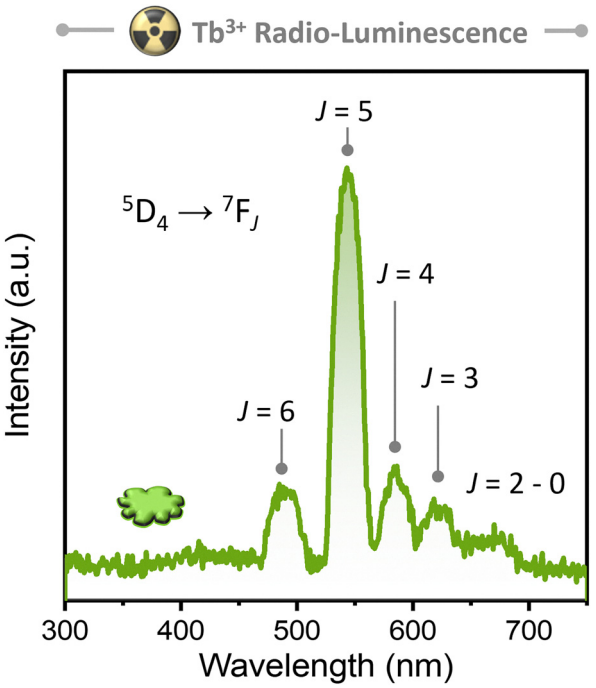

Fig. 7 X-ray excited optical luminescence (XEOL) spectrum of the Tb^{3+}-doped Gd_2O_2S flower-like nanostructures.

material.[6] In addition to Gd^{3+}-mediated excitation, the rather broad excitation band peaking at 298 nm might further indicate 4f–5d absorption of Tb^{3+}.[68] Following excitation and non-radiative decay to the Tb^{3+} ion's $^5D_4$ level, radiative decay down to the ^7F_J levels, with J = 6, 5, 4, and 3, takes place resulting in predominant green emission (Fig. 6E and F). As in case of upconversion, the flower-like nanostructures exhibited a significantly brighter emission, which can again be ascribed to surface quenching effects in the nano-platelets. Besides, further optimization of the dopant concentration or co-doping with Ce^{3+} (ref. 60) is expected to boost the emission intensity.

Radioluminescence of $Gd_2O_2S:Tb^{3+}$ nano-flowers. To assess the capability of the synthesized Tb^{3+}-doped Gd_2O_2S nanostructures to act as nano-scintillators, XEOL spectroscopy was performed, using a custom-made system (Fig. 7).[39] No luminescence was detected for Tb^{3+}/Yb^{3+}-doped nano-triangles, which could be related to surface quenching effects given the platelet-like morphology or sub-optimal Ln^{3+} dopant combinations as well as concentrations. This absence of X-ray excited luminescence in the Tb^{3+}/Yb^{3+} system may also correlate with the overall lower luminescence intensity observed for the same system under UV excitation (Fig. 6E), suggesting intrinsic limitations in the energy transfer processes. Conversely, in case of Tb^{3+}-doped flower-like nanostructures, the XEOL spectra showed a similar profile as the photoluminescence emission spectra (Fig. 6E) with emission bands stemming from the Tb^{3+} $^5D_4 \rightarrow {}^7F_J$ (J = 6–0) transitions.[35] Despite the relatively weak emission intensity, these preliminary results act as a stepping stone towards further exploration and optimization of dispersible nano-scintillators, including full XEOL experiments to understand and overcome quenching mechanisms.

Conclusions

In summary, we successfully synthesized lanthanide-doped gadolinium oxysulfide nanostructures, $Gd_2O_2S:Ln^{3+}$ (Ln = Yb, Er, Tb), *via* a microwave-assisted approach. The developed synthesis route allows to achieve crystalline and colloidal nanostructures within significantly reduced reaction times, *i.e.*, 20 min, compared to conventional methods. Moreover, the established strategy does not require any post-thermal treatment at elevated temperature in sulphur-containing atmosphere, nor the synthesis of complex molecular precursors as sulphur source. Instead, elemental sulphur has been applied in combination with lanthanide acetates ($Ln(OAc)_3$) and sodium oleate. Elemental analysis confirmed the formation of $Gd_2O_2S:Ln^{3+}$ with a homogenous distribution of dopant ions, although sulphur deficiencies were observed, particularly in the triangular morphologies, in agreement with previous reports on two-dimensional Ln_2O_2S. Raman spectroscopy, XRD, and FFT (high-resolution TEM) analysis further confirmed the phase purity and elemental composition of the obtained nanomaterials up to a Ln-to-S ratio of 1 : 4. At higher sulphur content, S-induced polymeric species were identified as secondary crystalline phase, which are suggested to further impact the morphological development of the nanostructures, *e.g.*, fostering their aggregation.

As a key finding, our study demonstrates that the morphology and phase purity of the resultant $Gd_2O_2S:Ln^{3+}$ nanostructures are highly dependent on the lanthanide-to-sulphur and sodium-to-lanthanide ratios. Stringent control of the precursor chemistry and reaction conditions resulted in the selective formation of nano-triangles, exhibiting a platelet-like two-dimensional morphology, over berry- and flower-like nanostructures. Herein, the systematic variation of the reaction parameters revealed a transition from small spherical nanoparticles to triangular platelets, and ultimately, to berry- and flower-like nanostructures, emphasizing the critical role of sulphur concentration in shaping the final morphology. While irregularly shaped platelet-like $Gd_2O_2S:Ln^{3+}$ nanostructures have previously been reported, to the best of our knowledge, this is the first isolation of nano-triangles.

Beyond structural characterization, the optical properties of the synthesized nanostructures were investigated. Co-doping with Er^{3+}/Yb^{3+} endowed the nanostructures with the upconverting and near-infrared (NIR) emitting properties characteristic for this ion pair under 980 nm NIR excitation. Doping of the nano-triangles and flower-like structures with Tb^{3+}/Yb^{3+} and Tb^{3+}, respectively, allowed for the detection of the characteristic green emission of Tb^{3+} under UV illumination. Moreover, first investigations unveiled X-ray excited optical luminescence (XEOL) from $Gd_2O_2S:Tb^{3+}$ nano-flowers, opening interesting opportunities towards nano-scintillators.

Overall, our findings highlight the advantages of microwave-assisted synthesis in achieving rapid and controlled Ln_2O_2S nanostructure formation. The tunability of morphology *via* reaction parameters and precursor chemistry provides a valuable framework for optimizing Gd_2O_2S-based materials for future applications in photonic and biomedical technologies.

Future work will focus on refining synthetic conditions to enhance the optical and scintillating performance of these nanostructures for their practical applications, for instance, fine-tuning of the concentration of the Ln^{3+} dopants (*e.g.*, Yb^{3+}, Er^{3+}) to improve energy transfer efficiency and emission intensity, particularly in morphologies where quenching effects are minimized, while also exploring alternative dopants that undergo upconversion and NIR emission. Although synthetically more challenging, targeting core/shell structures or seed-mediated growth may offer a route to suppress surface-related non-radiative losses and enhance luminescence efficiency. With respect to future applications, *e.g.*, in biomedicine or optoelectronics, surface ligands and opportunities for post-synthetic treatments are expected to open new opportunities. Leveraging the two-dimensional morphology of the Ln_2O_2S nanostructures, future research might explore single-particle emission behaviour, whereas, similar to $LiYF_4$ systems, anisotropic emission could be expected and may reveal properties not evident in ensemble measurements.[69,70] Alternatively, the here proposed nanostructures may serve as building blocks for integration into optoelectronic devices, *e.g.*, for applications ranging from analogue vision systems to electromagnetic absorbers.[71,72]

Author contributions

C. Homann: conceptualization, supervision, data curation, formal analysis, writing – original draft, writing – review & editing. R. Peeters: methodology, data curation, formal analysis, visualization. H. Mirmajidi: investigation, data curation, visualization. J. Berg: methodology, data curation, formal analysis, visualization. M. Fay: investigation, formal analysis, visualization. L. C. V. Rodrigues: investigation, formal analysis, data curation, writing – review & editing. E. Radicchi: investigation, data curation, formal analysis. A. Jain: investigation, formal analysis, data curation. A. Speghini: formal analysis, writing – review & editing. E. Hemmer: conceptualization, methodology, funding acquisition, supervision, writing – review & editing.

Conflicts of interest

There are no conflicts to declare.

Data availability

The data supporting this article have been included as part of the SI. Any additional information can be obtained from the corresponding authors upon reasonable request.

Additional experimental details; additional TEM images, Raman spectra, and XRD patterns of Er^{3+}/Yb^{3+}-, Tb^{3+}/Yb^{3+}-, and Tb^{3+}-doped Gd_2O_2S nanostructures; EDS elemental mapping; additional NIR emission. See DOI: **https://doi.org/10.1039/d5tc01646k**

Acknowledgements

The authors gratefully acknowledge the financial support provided by the Canada Foundation for Innovation (CFI), the National Research Council Canada (NRC, QSP 045-1), and the Natural Sciences and Engineering Research Council of Canada (NSERC, RGPIN-2023-03985). MF acknowledges the support of the Engineering and Physical Sciences Research Council (EPSRC) [under grant EP/W006413/1]. AJ acknowledges The Royal Society for the research grant (ref. no. RG\R1\251286). LCVR thanks Prof. Neilo Marcos Trindade and M.Sc. Matheus Cavalcanti dos Santos Nunes from the Institute of Physics (USP) for the XEOL setup and their aid in the XEOL measurements and acknowledges funding from FAPESP (grants #2019/05915-3, #2023/18315-0, #2024/03006-4, #2021/08111-2, and #2022/11983-4). AS and ER acknowledge the Center of Technological Platforms (Centro Piattaforme Tecnologiche, CPT) of the University of Verona for the use of the experimental Raman and XRD facilities and for technical support.

Notes and references

1 S. P. Wang, O. Laudi, H. Lucks, K. A. Wickersheim and R. A. Buchanan, X-ray image intensifier tubes using rare earth oxysulfide phosphors, *IEEE Trans. Nucl. Sci.*, 1970, **17**, 49–56.

2 B. K. Cha, J. Y. Kim, T. J. Kim, C. Sim and G. Cho, Fabrication and imaging characterization of high sensitive CsI(Tl) and Gd_2O_2S(Tb) scintillator screens for X-ray imaging detectors, *Radiat. Meas.*, 2010, **45**, 742–745.

3 L. Chen, Y. Wu, H. Huo, B. Tang, X. Ma, J. Wang, C. Sun, J. Sun and S. Zhou, Nanoscale Gd_2O_2S:Tb scintillators for high-resolution fluorescent imaging of cold neutrons, *ACS Appl. Nano Mater.*, 2022, **5**, 8440–8447.

4 K. E. Yorov, S. Nematulloev, B. M. Saidzhonov, M. S. Skorotetcky, A. A. Karluk, B. E. Hasanov, W. J. Mir, T. Sheikh, L. Gutiérrez-Arzaluz, M. E. M. Phielepeit, N. Ashraf, R. H. Blick, O. F. Mohammed, M. Bayindir and O. M. Bakr, Controlled synthesis of terbium-doped colloidal Gd_2O_2S nanoplatelets enables high-performance X-ray scintillators, *ACS Nano*, 2024, **18**, 20111–20122.

5 R. Martín-Rodríguez, F. T. Rabouw, M. Trevisani, M. Bettinelli and A. Meijerink, Upconversion dynamics in Er^{3+}-doped Gd_2O_2S: Influence of excitation power, Er^{3+} concentration, and defects, *Adv. Opt. Mater.*, 2015, **3**, 558–567.

6 J. Miranda de Carvalho, C. C. S. Pedroso, I. P. Machado, J. Hölsä, L. C. V. Rodrigues, P. Głuchowski, M. Lastusaari and H. F. Brito, Persistent luminescence warm-light LEDs based on Ti-doped RE_2O_2S materials prepared by rapid and energy-saving microwave-assisted synthesis, *J. Mater. Chem. C*, 2018, **6**, 8897–8905.

7 L. Lei, S. Zhang, H. Xia, Y. Tian, J. Zhang and S. Xu, Controlled synthesis of lanthanide-doped Gd_2O_2S nanocrystals with novel excitation-dependent multicolor emissions, *Nanoscale*, 2017, **9**, 5718–5724.

8 J. Santelli, S. Lechevallier, D. Calise, D. Marsal, A. Siegfried, M. Vincent, C. Martinez, D. Cussac, R. Mauricot and M. Verelst, Multimodal gadolinium oxysulfide nanoparticles for bioimaging: A comprehensive biodistribution, elimination and toxicological study, *Acta Biomater.*, 2020, **108**, 261–272.

9 J. Chen, Y. Song, D. Li, Q. Ma, X. Dong, W. Yu, X. Wang, Y. Yang, J. Wang and G. Liu, Investigating efficient energy transfer in novel strategy-obtained $Gd_2O_2S:Dy^{3+},Eu^{3+}$ nanofibers endowed with white emitting and magnetic dual-functionality, *J. Lumin.*, 2019, **206**, 509–517.

10 S. A. Osseni, S. Lechevallier, M. Verelst, P. Perriat, J. Dexpert-Ghys, D. Neumeyer, R. Garcia, F. Mayer, K. Djanashvili, J. A. Peters, E. Magdeleine, H. Gros-Dagnac, P. Celsis and R. Mauricot, Gadolinium oxysulfide nanoparticles as multimodal imaging agents for T_2-weighted MR, X-ray tomography and photoluminescence, *Nanoscale*, 2014, **6**, 555–564.

11 R. Martin-Rodriguez, S. Fischer, I. Aruna, B. Froehlich, K. W. Kraemer, J. C. Goldschmidt, B. S. Richards and A. Meijerink, Highly efficient IR to NIR upconversion in $Gd_2O_2S:Er^{3+}$ for photovoltaic applications, *Chem. Mater.*, 2013, **25**, 1912–1921.

12 Y. Ma, A. Aierken, Y. Wang and A. Meijerink, Dual functionality luminescence thermometry with $Gd_2O_2S:Eu^{3+},Nd^{3+}$ and its multiple applications in biosensing and *in situ* temperature measurements, *J. Colloid Interface Sci.*, 2023, **638**, 640–649.

13 A. R. Pessoa, J. A. O. Galindo, T. Possmayer, A. M. Amaral, M. Verelst, S. A. Maier and L. D. S. Menezes, Luminescence thermometry with Gd_2O_2S: Yb^{3+}/Er^{3+} nanoparticles under different excitation pathways, *Opt. Mater.*, 2024, **153**, 115574.

14 Q. Zou, C. Marcelot, N. Ratel-Ramond, X. Yi, P. Roblin, F. Frenzel, U. Resch-Genger, A. Eftekhari, A. Bouchet, C. Coudret, M. Verelst, X. Chen, R. Mauricot and C. Roux, Heterogeneous oxysulfide@fluoride core/shell nanocrystals for upconversion-based nanothermometry, *ACS Nano*, 2022, **16**, 12107–12117.

15 A. Cosgun Ergene, E. Madirov, E. Coetsee-Hugo, H. Swart, B. S. Richards and A. Turshatov, Extended range of ratiometric luminescence codes with Ce^{3+} modified $Gd_2O_2S:Er^{3+},Yb^{3+}$ shortwave infrared phosphors, *Adv. Opt. Mater.*, 2024, **12**, 2400925.

16 B. A. Wuille Bille and J. M. Velázquez, From Ln_2O_2S to $Ln_{10}OS_{14}$: exploring the sulphur spectrum of trivalent lanthanoid oxysulphides, *Dalton Trans.*, 2024, **53**, 6855–6859.

17 F. Ai, S. Goel, Y. Zhan, H. F. Valdovinos, F. Chen, T. E. Barnhart and W. Cai, Intrinsically ^{89}Zr-labeled $Gd_2O_2S:Eu$ nanophosphors with high in vivo stability for dual-modality imaging, *Am. J. Transl. Res.*, 2016, **8**, 5591–5600.

18 J. Sun, Y. Du, Z. Luo, H. Guo, Y. Liu, P. Sun and J. Jiang, Enhanced X-ray imaging with $Gd_2O_2S:Pr$-epoxy composite films: Synthesis, high-resolution performance, and flexibility, *ACS Appl. Electron. Mater.*, 2024, **6**, 2782–2787.

19 K. Matsumoto, T. Numazawa, Y. Ura, T. Ujiyama and S. Abe, Thermal and magnetic properties of regenerator material Gd_2O_2S, *J. Phys. Conf. Ser.*, 2017, **897**, 012010.

20 Q. Zou, L. Passini, L. Gibot, D. Lagarde, J. Hu, H. Zhu, F. Desmoulin, P. Sicard, N. Paiyabhroma, M. Verelst, R. Mauricot and C. Roux, PVP-coated ultrasmall Nd-doped Gd_2O_2S nanoparticles for multimodal imaging, *Mater. Chem. Front.*, 2023, **7**, 4109–4119.

21 H. Chen, T. Moore, B. Qi, D. C. Colvin, E. K. Jelen, D. A. Hitchcock, J. He, O. T. Mefford, J. C. Gore, F. Alexis and J. N. Anker, Monitoring pH-triggered drug release from radioluminescent nanocapsules with X-ray excited optical luminescence, *ACS Nano*, 2013, **7**, 1178–1187.

22 B. Ward-O'Brien, E. J. Pickering, R. Ahumada-Lazo, C. Smith, X. L. Zhong, Y. Aboura, F. Alam, D. J. Binks, T. L. Burnett and D. J. Lewis, Synthesis of high entropy lanthanide oxysulfides *via* the thermolysis of a molecular precursor cocktail, *J. Am. Chem. Soc.*, 2021, **143**, 21560–21566.

23 Y. Song, H. You, Y. Huang, M. Yang, Y. Zheng, L. Zhang and N. Guo, Highly uniform and monodisperse $Gd_2O_2S:Ln^{3+}$ (Ln = Eu, Tb) submicrospheres: Solvothermal synthesis and luminescence properties, *Inorg. Chem.*, 2010, **49**, 11499–11504.

24 F. Zhao and S. Gao, Pyrolysis of single molecular precursor for monodisperse lanthanide sulfide/oxysulfide nanocrystals, *J. Mater. Chem. B*, 2008, **18**, 949–953.

25 H. Lin, Q. Luo, W.-Y. Tong, C. Jiang, R. Huang, H. Peng, L.-C. Zhang, J. Travas-Sejdic and C.-G. Duan, Facile preparation of rare-earth semiconductor nanocrystals and tuning of their dimensionalities, *RSC Adv.*, 2015, **5**, 86885–86890.

26 Y. Zhan, F. Ai, F. Chen, H. F. Valdovinos, H. Orbay, H. Sun, J. Liang, T. E. Barnhart, J. Tian and W. Cai, Intrinsically zirconium-89 labeled $Gd_2O_2S:Eu$ nanoprobes for in vivo positron emission tomography and gamma-ray-induced radioluminescence imaging, *Small*, 2016, **12**, 2872–2876.

27 C. Larquet, D. Carriere, A.-M. Nguyen, T. K.-C. Le, X. Frogneux-Plé, I. Génois, P. Le Griel, A. Gauzzi, C. Sanchez and S. Carenco, Unraveling the role of alkali cations in the growth mechanism of Gd_2O_2S nanoparticles, *Chem. Mater.*, 2020, **32**, 1131–1139.

28 S.-L. Lin, T.-Y. Liu, C.-L. Lo, B.-S. Wang, Y.-J. Lee, K.-Y. Lin and C. A. Chang, Synthesis, surface modification, and photophysical studies of $Ln_2O_2S:Ln^{3+}$ (Ln = Gd, Tb, Eu; Ln = Tb and/or Eu) nanoparticles for luminescence bioimaging, *J. Lumin.*, 2016, **175**, 165–175.

29 J. Thirumalai, R. Chandramohan, S. Valanarasu, T. A. Vijayan, R. M. Somasundaram, T. Mahalingam and S. R. Srikumar, Shape-selective synthesis and opto-electronic properties of Eu^{3+}-doped gadolinium oxysulfide nanostructures, *J. Mater. Sci.*, 2009, **44**, 3889–3899.

30 C. d Angel-Olarte, L. Hernández-Adame, A. Mendez-Blas and G. Palestino, Eu^{3+}/Yb^{3+} co-doped gadolinium oxysulfide upconverting nanorods: Morphological, physicochemical and optical evaluation, *J. Alloys Compd.*, 2019, **787**, 1032–1043.

31 J. Thirumalai, R. Chandramohan, R. Divakar, E. Mohandas, M. Sekar and P. Parameswaran, Eu^{3+} doped gadolinium oxysulfide (Gd_2O_2S) nanostructures—synthesis and optical and electronic properties, *Nanotechnology*, 2008, **19**, 395703.

32 I. Bilecka and M. Niederberger, Microwave chemistry for inorganic nanomaterials synthesis, *Nanoscale*, 2010, **2**, 1358–1374.
33 C. Homann, N. Liu, H. Barbosa and E. Hemmer, in *Handbook on the Physics and Chemistry of Rare Earths*, ed. J.-C. G. Bünzli and S. M. Kauzlarich, Elsevier, 2024, vol. 65, pp. 137–212.
34 I. P. Machado, J. de Wit, A. J. van Bunningen, C. C. S. Pedroso, L. C. V. Rodrigues, H. F. Brito and A. Meijerink, Highly luminescent $Gd_2O_2S:Er^{3+},Yb^{3+}$ upconversion microcrystals obtained by a time- and energy-saving microwave-assisted solid-state synthesis, *J. Alloys Compd.*, 2023, **942**, 169083.
35 I. P. Machado, V. C. Teixeira, C. C. S. Pedroso, H. F. Brito and L. C. V. Rodrigues, X-ray scintillator $Gd_2O_2S:Tb^{3+}$ materials obtained by a rapid and cost-effective microwave-assisted solid-state synthesis, *J. Alloys Compd.*, 2019, **777**, 638–645.
36 C. He, Z. Xia and Q. Liu, Microwave solid state synthesis and luminescence properties of green-emitting $Gd_2O_2S:Tb^{3+}$ phosphor, *Opt. Mater.*, 2015, **42**, 11–16.
37 I. Halimi, E. M. Rodrigues, S. L. Maurizio, H.-Q. T. Sun, M. Grewal, E. M. Boase, N. Liu, R. Marin and E. Hemmer, Pick your precursor! Tailoring the size and crystal phase of microwave-synthesized sub-10 nm upconverting nanoparticles, *J. Mater. Chem. C*, 2019, **7**, 15364–15374.
38 N. Liu, C. Homann, S. Morfin, M. S. Kesanakurti, N. D. Calvert, A. J. Shuhendler, T. Al and E. Hemmer, Core-multi-shell design: Unlocking multimodal capabilities in lanthanide-based nanoparticles as upconverting, T_2-weighted MRI and CT probes, *Nanoscale*, 2023, **15**, 19546–19556.
39 M. C. S. Nunes, M. L. Rodrigues, W. J. R. Silva, R. S. Silva, N. K. Umisedo, E. M. Yoshimura and N. M. Trindade, A custom-made integrated system for thermoluminescence and radioluminescence spectroscopy, *Appl. Radiat. Isot.*, 2024, **214**, 111516.
40 M. Klinger, More features, more tools, more CrysTBox, *J. Appl. Cryst.*, 2017, **50**, 1226–1234.
41 A. Jain, S. P. Ong, G. Hautier, W. Chen, W. D. Richards, S. Dacek, S. Cholia, D. Gunter, D. Skinner, G. Ceder and K. A. Persson, The Materials Project: A materials genome approach to accelerating materials innovation, *APL Mater.*, 2013, **1**, 011002.
42 *The Materials Project, Materials Explorer, Gd_2SO_2 mp-4805, Database version v2025.06.09*, DOI: **10.17188/1208411**, **https://next-gen.materialsproject.org/materials/mp-4805**.
43 C. F. Holder and R. E. Schaak, Tutorial on powder X-ray diffraction for characterizing nanoscale materials, *ACS Nano*, 2019, **13**, 7359–7365.
44 H. X. Mai, Y. W. Zhang, R. Si, Z. G. Yan, L. D. Sun, L. P. You and C. H. Yan, High-quality sodium rare-earth fluoride nanocrystals: Controlled synthesis and optical properties, *J. Am. Chem. Soc.*, 2006, **128**, 6426–6436.
45 N. Liu, R. Marin, Y. Mazouzi, G. O. Cron, A. Shuhendler and E. Hemmer, Cubic versus hexagonal – Effect of host crystallinity on the T_1 shortening behaviour of $NaGdF_4$ nanoparticles, *Nanoscale*, 2019, **11**, 6794–6801.
46 B. Amouroux, C. Roux, J.-D. Marty, M. Pasturel, A. Bouchet, M. Sliwa, O. Leroux, F. Gauffre and C. Coudret, Importance of the mixing and high-temperature heating steps in the controlled thermal coprecipitation synthesis of sub-5-nm $Na(Gd–Yb)F_4$:Tm, *Inorg. Chem.*, 2019, **58**, 5082–5088.
47 Y. Ding, J. Gu, J. Ke, Y.-W. Zhang and C.-H. Yan, Sodium doping controlled synthesis of monodisperse lanthanide oxysulfide ultrathin nanoplates guided by density functional calculations, *Angew. Chem., Int. Ed.*, 2011, **50**, 12330–12334.
48 B. Ward-O'Brien, P. D. McNaughter, R. Cai, A. Chattopadhyay, J. M. Flitcroft, C. T. Smith, D. J. Binks, J. M. Skelton, S. J. Haigh and D. J. Lewis, Quantum confined high-entropy lanthanide oxysulfide colloidal nanocrystals, *Nano Lett.*, 2022, **22**, 8045–8051.
49 S. Ashoka Sahadevan, X. Xiao, Y. Ma, K. Forsberg, R. T. Olsson and J. M. Gardner, Sulfur–oleylamine copolymer synthesized *via* inverse vulcanization for the selective recovery of copper from lithium-ion battery E-waste, *Mater. Chem. Front.*, 2023, **7**, 1374–1384.
50 A. D. Smith, C. D. McMillen, R. C. Smith and A. G. Tennyson, Copolymers by inverse vulcanization of sulfur with pure or technical-grade unsaturated fatty acids, *J. Polym. Sci.*, 2020, **58**, 438–445.
51 S.-J. Lee, G.-Y. Han, M.-B. Yi, J.-H. Back and H.-J. Kim, From waste to tape: Inverse vulcanization of sulfur and solvent-based depolymerization for preparation of pressure-sensitive adhesives, *J. Mater. Res. Technol.*, 2024, **29**, 1798–1804.
52 C. Larquet, D. Hourlier, A.-M. Nguyen, A. Torres-Pardo, A. Gauzzi, C. Sanchez and S. Carenco, Thermal stability of oleate-stabilized Gd_2O_2S nanoplates in inert and oxidizing atmospheres, *ChemNanoMat*, 2019, **5**, 539–546.
53 N. M. Pirozzi, J. Kuipers and B. N. G. Giepmans, in *Methods in Cell Biology*, ed. T. Müller-Reichert and P. Verkade, Academic Press, 2021, vol. 162, pp. 89–114.
54 Y. Numata, H. Kobayashi, N. Oonami, Y. Kasai and H. Tanaka, Simultaneous determination of oleic and elaidic acids in their mixed solution by Raman spectroscopy, *J. Mol. Struct.*, 2019, **1185**, 200–204.
55 A. D. Smith, A. G. Tennyson and R. C. Smith, Sulfur-containing polymers prepared from fatty acid-derived monomers: Application of atom-economical thiol-ene/thiol-yne click reactions and inverse vulcanization strategies, *Sustainable Chem.*, 2020, **1**, 209–237.
56 L. J. Dodd, C. Lima, D. Costa-Milan, A. R. Neale, B. Saunders, B. Zhang, A. Sarua, R. Goodacre, L. J. Hardwick, M. Kuball and T. Hasell, Raman analysis of inverse vulcanised polymers, *Polym. Chem.*, 2023, **14**, 1369–1386.
57 S. Yokono, S. Imanaga and T. Hoshina, Raman spectra for Eu doped Ln_2O_2S phosphors, *J. Phys. Soc. Jpn.*, 1979, **46**, 1882–1888.
58 S. Zhang, J. Zhou, R. Wu, L. Lei, Z. Xiao, J. Zhang and S. Xu, Controlling red upconversion luminescence in $Gd_2O_3:Yb^{3+}$–Er^{3+} nanoparticles by changing the different atmosphere, *RSC Adv.*, 2016, **6**, 101707.

59 F. Zhao, M. Yuan, W. Zhang and S. Gao, Monodisperse lanthanide oxysulfide nanocrystals, *J. Am. Chem. Soc.*, 2006, **128**, 11758–11759.

60 N. Panov, R. Marin and E. Hemmer, Microwave-assisted solvothermal synthesis of upconverting and downshifting rare-earth-doped $LiYF_4$ microparticles, *Inorg. Chem.*, 2018, **57**, 14920–14929.

61 N. Liu, J. Holmes, N. Bordenave and E. Hemmer, Microwave-assisted synthesis of $NaMnF_3$ particles with tuneable morphologies, *Chem. Commun.*, 2021, **57**, 11799–11802.

62 P. N. Knüsel, A. Riedinger, A. A. Rossinelli, F. D. Ott, A. S. Mule and D. J. Norris, Experimental evidence for two-dimensional Ostwald ripening in semiconductor nanoplatelets, *Chem. Mater.*, 2020, **32**, 3312–3319.

63 I. Coropceanu, A. Rossinelli, J. R. Caram, F. S. Freyria and M. G. Bawendi, Slow-injection growth of seeded CdSe/CdS nanorods with unity fluorescence quantum yield and complete shell to core energy transfer, *ACS Nano*, 2016, **10**, 3295–3301.

64 V. Kataria, S. Dixit and D. S. Mehta, Investigations on the up/downconversion of Gd_2O_2S: Er, Yb nanophosphor with both excitation wavelength and Yb^{3+}-dependent emission color modulation, *J. Mater. Sci.*, 2019, **54**, 13635–13650.

65 F. Wang, Y. Han, C. S. Lim, Y. H. Lu, J. Wang, J. Xu, H. Y. Chen, C. Zhang, M. H. Hong and X. G. Liu, Simultaneous phase and size control of upconversion nanocrystals through lanthanide doping, *Nature*, 2010, **463**, 1061–1065.

66 N. Liu, N. Gobeil, P. Evers, I. Gessner, E. M. Rodrigues and E. Hemmer, Water dispersible ligand-free rare earth fluoride nanoparticles: Water transfer versus $NaREF_4$-to-REF_3 phase transformation, *Dalton Trans.*, 2020, **49**, 16204–16216.

67 N. Pawlik, T. Goryczka, B. Szpikowska-Sroka and W. A. Pisarski, The photoluminescence studies of Gd^{3+}/Tb^{3+} co-doped xerogels and nano-glass-ceramics dedicated for green-emitting devices, *Opt. Mater. X*, 2024, **23**, 100336.

68 S. Chatterjee, V. Shanker and H. Chander, Thermoluminescence of Tb doped Gd_2O_2S phosphor, *Mater. Chem. Phys.*, 2003, **80**, 719–724.

69 J. Zhou, A. I. Chizhik, S. Chu and D. Jin, Single-particle spectroscopy for functional nanomaterials, *Nature*, 2020, **579**, 41–50.

70 N. Panov, D. Lu, E. Ortiz-Rivero, E. Martinazzo Rodrigues, P. Haro-González, D. Jaque and E. Hemmer, Hyperspectral imaging and optical trapping: Complementary tools for assessing direction-dependent polarized emission from single upconverting $LiYF_4$:Yb^{3+}/Er^{3+} microparticles, *Adv. Opt. Mater.*, 2021, **9**, 2100101.

71 N. Li, B. Wen, X. Li, A. Zuo, S. Yang, S. Ding and G. Yang, High-quality ultrathin Gd_2O_2S nanosheets with oxygen vacancy-decorated rGO for enhanced electromagnetic wave absorption, *ACS Appl. Mater. Interfaces*, 2023, **15**, 53891–53901.

72 A. Dodda, D. Jayachandran, S. Subbulakshmi Radhakrishnan, A. Pannone, Y. Zhang, N. Trainor, J. M. Redwing and S. Das, Bioinspired and low-power 2D machine vision with adaptive machine learning and forgetting, *ACS Nano*, 2022, **16**, 20010–20020.